Materials Today Advances 21 (2024) 100464

Contents lists available at ScienceDirect

Materials Today Advances

journal homepage: www.journals.elsevier.com/materials-today-advances/

A new class of porous silicon electrochemical transducers built from pyrolyzed polyfurfuryl alcohol

Anandapadmanabhan A. Rajendran [a], Keying Guo [b], Alberto Alvarez-Fernandez [c], Thomas R. Gengenbach [d], Marina B. Velasco [a], Maximiliano J. Fornerod [c], Kandeel Shafique [a], Máté Füredi [c], Pilar Formentín [a], Hedieh Haji-Hashemi [a], Stefan Guldin [c], Nicolas H. Voelcker [e,f], Xavier Cetó [g], Beatriz Prieto-Simón [a,h,*]

[a] Department of Electronic Engineering, Universitat Rovira i Virgili, 43007, Tarragona, Spain
[b] Biological and Environmental Science and Engineering Division, King Abdullah University of Science and Technology, Thuwal, Saudi Arabia
[c] Department of Chemical Engineering, University College London, London, WC1E 7JE, UK
[d] Commonwealth Scientific and Industrial Research Organization (CSIRO), Clayton, Victoria, 3168, Australia
[e] Faculty of Pharmacy and Pharmaceutical Sciences, Monash University, Parkville, VIC, Australia
[f] Melbourne Centre for Nanofabrication, Victorian Node of the Australian National Fabrication Facility, Clayton, VIC, Australia
[g] Department of Chemistry, Universitat Autònoma de Barcelona, 08193, Bellaterra, Spain
[h] ICREA, Pg. Lluís Companys 23, 08010, Barcelona, Spain

ARTICLE INFO

Keywords:
Porous silicon
Carbon-stabilization
Polyfurfuryl alcohol
Electrochemical transducer
DNA sensor

ABSTRACT

Carbon-based nanomaterials are key to developing high-performing electrochemical sensors with improved sensitivity and selectivity. Nonetheless, limitations in their fabrication and integration into devices often constrain their practical applications. Moreover, carbon nanomaterials-based electrochemical devices still face problems such as large background currents, poor stability, and slow kinetics. To advance towards a new class of carbon nanostructured electrochemical transducers, we propose the in-situ polymerization and carbonization of furfuryl alcohol (FA) on porous silicon (pSi) to produce a tailored and highly stable transducer. The thin layer of polyfurfuryl alcohol (PFA) that conformally coats the pSi scaffold transforms into nanoporous carbon when subjected to pyrolysis above 600 °C. The morphological and chemical properties of PFA-pSi were characterized by scanning electron microscopy, and Raman and X-ray photoelectron spectroscopies. Their stability and electrochemical performance were investigated by cyclic voltammetry and electrochemical impedance spectroscopy in $[Fe(CN)_6]^{3-/4-}$, $[Ru(NH_3)_6]^{2+/3+}$, and hydroquinone. PFA-pSi showed superior electrochemical performance compared to screen-printed carbon electrodes while also surpassing glassy carbon electrodes in specific aspects. Besides, PFA-pSi has the additional advantage of easy tuning of the electroactive surface area. To prove its potential for biosensing purposes, a DNA sensor based on quantifying the partial pore blockage of the pSi upon target hybridization was built on PFA-pSi. The sensor showed a limit of detection of 1.4 pM, outperforming other sensors based on the same sensing mechanism.

1. Introduction

Recent advancements have taken the application of carbon-based nanomaterials to the next level with the development of diverse synthetic allotropes of carbon, such as graphene, carbon nanotubes (CNTs), carbon nanofibers, carbon dots (CDs) and carbon nanoparticles (CNPs). Carbon-based materials have become a common electrode material for electrochemical sensing due to their excellent electrical properties, chemical stability, and rich surface chemistry [1–3]. In electrochemistry, the performance of a transducer largely depends on the reaction between the electrode surface and the solution interface. Therefore, the electrode surface structure and its chemistry are important factors in determining the electrochemical reaction rate [4]. In this regard, carbon-based nanostructured materials have been exploited to develop electrochemical transducers. They are often used to modify and thereby improve the electrode properties, especially in the case of

* Corresponding author.
E-mail address: beatriz.prieto-simon@urv.cat (B. Prieto-Simón).

https://doi.org/10.1016/j.mtadv.2024.100464
Received 3 October 2023; Received in revised form 22 December 2023; Accepted 3 January 2024
Available online 12 January 2024

polycrystalline graphite electrodes such as pyrolytic graphite electrode (PGE) [5] and glassy carbon electrode (GCE) [6], along with commercial screen-printed carbon electrodes (SPCE) [7]. Eminently, such modifications not only improve the electrode sensitivity, but also the electrical conductivity and electrocatalytic performance [8,9]. Despite the several advantages that carbon materials may offer, their usage also involves some drawbacks. For instance, the large current response sparked by carbon nanomaterial-based electrodes evokes background noise that can hamper the electrode performance in sensing applications [10]. Background noise is even more significant for pure carbon nanomaterials, where extensive reduction of the carbon surface is required to generate oxygenated reactive sites for sensing [10,11]. Also, the orientation and arrangement of certain carbon materials (*e.g.*, CNTs) on the electrode surface significantly affect the electron transfer rate [4]. This is because in such materials the reactivity of atoms differs at the edge/plane sites [11]. In addition, certain types of carbon-based materials are vulnerable to oxidative environment. Lanza *et al.* reported that defects in the boundaries of graphene sheets can suffer local oxidation in a disordered way even at room temperature. Such oxidative effect significantly reduces the material conductivity and mechanical resistance [12]. Moreover, the tedious synthesis, high fabrication cost, tendency to aggregate and often-unknown levels of defects arising during fabrication make the development of efficient electrochemical transducers based on carbon nanomaterials rather challenging [13–16].

Hence, there is a need for novel electrochemical transducers that can overcome the challenges emerging from existing transducers. "Ideal" electrochemical transducers must be characterized by low background currents, wide potential window, fast electron transfer kinetics, high effective electrode area, and excellent reproducibility and stability [17].

Following this direction, a new breed of electrode architecture based on carbon-stabilized porous silicon (pSi) has been recently studied [18,19]. The potential of using pSi to build electrode architectures relies on its unique properties, especially its readily tunable pore morphology (*e.g.*, pore size and depth, porosity), high surface area ($>100\ m^2cm^{-2}$), and a versatile surface chemistry affording ease of functionalization [20–26]. By simply tuning the etching parameters *viz*. current density, etching time, or etchant ratio, the pore morphology can be adjusted to meet the desired needs [22,27,28].

Despite such advantageous features, the use of pSi as electrochemical transducer is still limited, with a very few studies published. One of the main challenges is the poor stability of hydride-terminated freshly etched pSi, that is prone to oxidation in both water and air [27]. Although there are many chemical modifications reported to stabilize pSi (*e.g.*, thermal oxidation [29], hydrosilylation [30], electrochemical alkylation [31]), they limit pSi performance as electrochemical transducer. Notably, Salonen *et al.* pioneered a method of *in-situ* thermal decomposition of acetylene gas for the generation of two carbon-stabilized pSi nanostructures: thermally hydrocarbonized pSi (THC-pSi) and thermally carbonized pSi (TC-pSi) [18]. The carbon layer protects pSi from surface degradation and enables crafting its surface chemistry to facilitate immobilization of biomolecules, hence gathering attention towards (bio)chemical sensing applications [32]. This study paved the way for harnessing those carbon-stabilized pSi structures as electrodes featuring a large surface area-to-volume ratio, and thus being able to deliver outstanding sensitivity.

More recently, Guo *et al.* reported on the potential of THC-pSi and TC-pSi as novel electrochemical transducers [20]. Both platforms showed large effective electrode area, and excellent electrochemical performance and stability [20,22].

Additional strategies have been developed to generate conformal carbon coatings on pSi. As aforementioned, not only does carbon directly bonded to silicon yield a very stable surface, but also a new material owning fast electron transfer kinetics. To this end, Sailor *et al.* reported a method of thermally carbonizing pSi using furfuryl alcohol (FA). In that work, a highly stable mesoporous carbon coating was formed on pSi by extensive pyrolysis of polyfurfuryl alcohol (PFA), polymerized *in situ* in a pSi template [33]. Added to endowing pSi with high stability, it was found that the mesoporous carbon coating significantly improved the sensitivity of the carbon/Si composite for optical organic vapor sensing [33].

PFA is a thermally cross-linked polymer that generates nanoporous carbon (NpC) when pyrolyzed above 600 °C [33]. PFA has often been the precursor choice to produce nanostructured carbon materials and carbon-based nanocomposites for applications such as molecular sieve adsorbents, catalyst supports or ultracapacitors [34–38]. The temperature-dependence of PFA electrical conductivity has been extensively investigated [38]. Increasing pyrolysis temperature not only promotes charge carriers (holes) mobility by connecting neighboring smaller conducting domains into larger ones, but also efficiently creates charge carriers by degrading PFA molecules. This agrees with previous reports that attribute the conduction in disordered carbon materials to the presence of holes acting as charge carriers, created by heating carbonaceous materials at temperatures between 500 and 1000 °C [38–40]. Thus, exploiting PFA advantages as powerful carbon nanomaterial, and combining them with tunable pSi's features could yield a highly efficient electrochemical transducer. While PFA optical and electronic properties have been thoroughly studied, its relevance in electrochemistry is yet to be explored.

Here, we report a novel carbon-stabilized pSi device, prepared through the polymerization and carbonization of FA infiltrated within pSi to introduce a conformal conductive layer suitable as a nanostructured electrochemical transducer with unique advantages. Unlike electrochemical transducers based on carbon nanomaterials, PFA-pSi is a highly stable transducer with a straightforward fabrication process. Freshly etched pSi was first modified with FA by spin coating, and later subjected to thermal heating for polymerization and carbonization. The morphological, chemical and electrochemical properties of PFA-pSi were extensively studied. Its electrochemical performance was benchmarked against commercial SPCE and GCE, and also against other nanostructured carbon-stabilized pSi platforms previously reported (*i.e.*, THC-pSi, TC-pSi).

Finally, PFA-pSi's potential for electrochemical (bio)sensing was underpinned by developing and optimizing a PFA-pSi-based DNA sensor. The excellent electrochemical performance of PFA-pSi along with its ease of functionalization highlights its potential as a novel nanostructured electrode.

2. Experimental section

2.1. Reagents

Hydrofluoric acid (HF) (48 %, AR grade), absolute ethanol, sodium hydroxide (NaOH), potassium ferrocyanide ($K_4[Fe(CN)_6]$), potassium ferricyanide ($K_3[Fe(CN)_6]$), furfuryl alcohol (FA), oxalic acid, 4-aminobenzoic hydrazide (4-ABH), sodium nitrite ($NaNO_2$), phosphate-buffered saline (PBS) tablets, Tris-HCl, sodium chloride (NaCl), and ethanolamine hydrochloride were purchased from Sigma-Aldrich (Spain). P-type Si wafers with 0.00055–0.001 Ω cm resistivity, (100)-oriented were purchased from Siltronix (France). All the DNA strands were purchased from Integrated DNA Technologies S.L. (Spain). The sequence of the amino-modified ssDNA capture probe was 5'-/5AmMC6/AGT TAT CCC AGT CTT ATA GGT AGG T-3'. The amino-modified non-specific ssDNA capture probe was 5'-/5AmMC6/GTC CAC GCC GTA AAC GAT GTC GAC TTG G-3'. The sequence of the target ssDNA was 5′- ACC TAC CTA TAA GAC TGG GAT AAC T-3'.

2.2. PSi fabrication

PSi was fabricated from p-type Si wafers with 0.00055 Ω cm resistivity, and ⟨100⟩-oriented conditions propagating primarily in this direction. Fabrication was performed via electrochemical etching by anodizing the Si substrate in two steps. Anodization needs two

electrodes to maintain charge neutrality and to close the electrical circuit. A platinum electrode (cathode) supplies electrons to the etching solution, and the Si wafer (anode) removes electrons from the solution. The etching solution consisted of HF as an etchant and ethanol as a surfactant or wetting agent, which lowers the surface tension of the etching solution and helps HF to access the surface.

First, the sample was electropolished with a current density of 350 mA for 30 s in a 3:1 (v/v) solution of aqueous HF (48 %) and absolute ethanol, to etch the sacrificial layer. The sacrificial layer was dissolved by replacing the electrolyte with a 2 M aqueous solution of NaOH for a few min, and the clean Si was then rinsed with ethanol. The second anodization was performed under a current of 72 mA for 100 s using a 1:1 (v/v) solution of aqueous HF (48 %) and ethanol. Passing an electric current through the Si wafer led to the dissolution of Si atoms and the removal of surface roughness when a critical current density was exceeded. As the wafer was soaked in HF, uniform porosity and thickness of the Si surface were achieved.

2.3. Polymerization of FA on pSi and PFA carbonization

Freshly etched pSi samples were modified with FA by spin coating. 20 % FA by volume was prepared in absolute ethanol containing 5.0 mg mL^{-1} oxalic acid used as catalyst. Spin coating was done in two steps where two angular velocity conditions were applied. First, the spin coating was done at 700 rpm for 2 min to infiltrate FA into the porous structure. Next, the spinning was increased to 4000 rpm for 1 min. Subsequently, to generate carbon-infiltrated pSi composites, FA-coated pSi samples were placed into a quartz tube under N_2 flow. First, the temperature was increased 5 °C min^{-1} until reaching a temperature of 100 °C to polymerize FA. This temperature was maintained for 2 h and then increased 15 °C min^{-1} up to 700 °C to form a carbon composite. At this time, the temperature was constant for 2 h and 20 min. Finally, the tube cooled back to room temperature under N_2 flow.

2.4. Field-emission scanning electron microscopy (FESEM)

FESEM was used to characterize specific properties of the fabricated pSi samples. FESEM (Scios 2 from FEI Company) imaging was carried out at an accelerating voltage of 5 kV to confirm both pore size and thickness of the samples.

2.5. Optical tensiometer

The water contact angle measurement on pSi and PFA-pSi was performed using an Attension theta lite optical tensiometer (basic model with manual dispenser and droplet placement) from Biolin scientific, (Gothenburg, Sweden). Images of water droplets (1 μL) with a 1 mL syringe at four different spots on the surface of the sample were taken. One Attension software was used to analyze the surface contact angle of the water drop.

2.6. Spectroscopic ellipsometry (SE)

SE measurements were carried out on a Semilab SE2000 variable angle spectroscopic ellipsometer in the spectral range from 300 to 900 nm. The obtained values for amplitude component (Ψ) and phase difference (Δ) were subsequently analyzed using the Semilab's SEA software (v1.6.2) using the Cauchy dispersion law to determine the layer thickness and refractive index, from which the relative porosity of the surface structure was estimated using the Bruggeman effective medium approximation.

2.7. Optical interference spectroscopy

Reflectance spectra were obtained using a Perkin Elmer UV–visible–NIR lamda 950 spectrophotometer. Incident light of 8° was focused through a lens onto the porous films. The reflectivity spectra were recorded in the range from 300 to 1200 nm, with NIR resolution of 2 nm. MATLAB program was applied to the resulting spectra to obtain the single peak position corresponding to effective optical thickness (EOT).

2.8. Fourier transform infrared spectroscopy (FTIR)

FTIR spectra were recorded on a Jasco FTIR-4000 series using transmission and reflectance modes. All spectra were recorded at an average of 64 scans within a range from 400 to 4000 cm^{-1}. The spectra were then plotted using Origin software.

2.9. X-ray photoelectron spectroscopy (XPS)

XPS spectra were recorded using a K-alpha spectrometer equipped with a monochromated, micro-focused, Al K-Alpha X-ray source (1486.6 eV), a quartz crystal monochromator set in a 250-mm Rowland circle, hybrid optics, multichannel plate, hemispherical analyzer and 128-channel sensitive detector. The incident and collection angles were 30° and 0°, respectively, comparative to the surface normal. The base pressure was 10^{-9} mbar and 180° double-focusing hemispherical analyzer having mean radius 125 mm which was run in constant analyzer energy mode. The pass energies were set to 20 eV for high resolution and 80 eV for survey scans.

2.10. Raman spectroscopy

A Renishaw inVia Raman microscope with a 100 mW 532 nm laser excitation source was used to acquire Raman spectra. To avoid the damage of the sample surface, a 10 % excitation power density was applied. The band deconvolution of the Raman spectra was performed using Origin software.

2.11. Electrochemical measurements

Electrochemical measurements were carried out with an electrochemical potentiostat (Ivium-n-Stat, s module 2.5 A/10 V) using a three-electrode electrochemical cell.

Cyclic voltammetry (CV) measurements were performed, at a scan rate of 100 mV s^{-1}. Electrochemical impedance spectroscopy (EIS) measurements were recorded in a 2 mM $[Fe(CN)_6]^{3-/4-}$ solution prepared in PBS buffer (140 mM NaCl, 10 mM phosphate buffer and 3 mM KCl, pH 7.4) at an open circuit potential of 0.2 V and scanning from 100 kHz to 100 mHz, with a fixed AC amplitude of 10 mV.

All the data and analysis were done using Ivium-n-Stat Instrument software (Ivium Technologies B.V., Eindhoven, Netherlands). DropSens electrodes (110) were used as SPCE. For PFA-pSi, the working electrode area was delimited to 7.4 mm diameter by an O-ring present in an in-house built Teflon cell. For both SPCE and PFA-pSi an external Ag/AgCl (3 M NaCl) electrode and a platinum wire were used as reference and counter electrodes, respectively. For the measurements, all the electrodes were placed into a Faraday cage.

2.12. Electrografting with 4-aminobenzoic hydrazide

Hydrazide groups were introduced on pSi by electrografting a diazonium salt generated from 4-ABH. 5 mM aqueous solution of $NaNO_2$ was mixed with 10 mM 4-ABH prepared in 0.5 M HCl in a ratio of 1:2 (v/v), which was left to react for 30 min in ice, prior to the electrografting process. The electrochemical reductive modification of the PFA-pSi was conducted by CV, by scanning the potential between −0.6 and 0.6 V at 100 mV s^{-1} for 20 scans [41,42]. Subsequently, functionalized PFA-pSi electrodes were rinsed with 10 mM PBS (pH 7.4) and then subjected to potential scanning between −0.2 and 0.6 V for 10 cycles at 100 mV s^{-1} to remove any physisorbed compounds.

2.13. Covalent immobilization of ssDNA

Once the PFA-pSi surface was functionalized with hydrazide groups, the next step was to bring in a bifunctional linker molecule. The hydrazide-modified PFA-pSi surface was immersed in a freshly prepared solution of 2.5 % glutaraldehyde in 10 mM PBS for 1 h to allow further immobilization of the amine-modified ssDNA capture probes. A 0.5 μM DNA capture probe solution prepared in 10 mM PBS was incubated on the aldehyde-terminated surface overnight at 4 °C. Next, 0.1 M ethanolamine prepared in 10 mM PBS was incubated for 1 h on the sensor surface to block any remaining aldehyde groups.

2.14. Electrochemical sensing protocol for the DNA sensor

Solutions of the target ssDNA were prepared in 10 mM Tris buffer with 75 mM NaCl (pH 7.4) at the following concentrations: 0.1 pM, 10 pM, 100 pM and 1000 pM. These solutions were incubated on both PFA-pSi sensors and controls (sensors modified with a random sequence) for 30 min. EIS was used as the electrochemical detection technique to quantify the partial pore blockage caused upon DNA hybridization. EIS measurements of five PFA-pSi sensors and five PFA-pSi control samples were performed in 2 mM $[Fe(CN)_6]^{3-/4-}$ solution in 10 mM PBS buffer at pH 7.4, prior and after target incubation. After every incubation, both PFA-pSi sensors and controls were thoroughly rinsed with 10 mM Tris buffer containing 75 mM NaCl (pH 7.4).

2.15. Statistical analysis

All the figures related to chemical characterization and electrochemical characterization of PFA-pSi were plotted using Origin 9 software. Graph Pad prism 8 was used to quantify all statistical analysis using t-test. The data obtained from all measurements (n = 5) were presented as mean ± standard error mean.

3. Results and discussion

3.1. Fabrication and characterization of pSi modified via pyrolysis of PFA

PSi was fabricated via two-step electrochemical anodization of boron-doped (p-type) crystalline Si (100) in the presence of hydrofluoric acid (HF) and ethanol. Freshly etched pSi was then subjected to coating of FA by spin coating in two angular velocity conditions. First, the spin coating was conducted at 700 rpm for 2 min to infiltrate FA into the porous structure. Next, the spinning was increased to 4000 rpm for 1 min to remove any excess of FA. This was followed by pyrolysis of FA at 700 °C. This process introduced a carbon layer on the pSi surface, therein stabilizing and rendering pSi electrically conductive (shown in Fig. 1).

3.1.1. Morphological characterization

The pore morphology and film thickness of both freshly etched pSi and PFA-pSi were investigated using FESEM. Fig. 2a and c shows the top and cross-sectional FESEM images of freshly etched pSi. Samples etched for 100 s with a current density of 43 mA cm^{-2}, showed an average pore diameter of 60 ± 18 nm and a layer thickness of 2.3 ± 0.3 μm. After PFA pyrolysis, the layer thickness was retained (Fig. 2d), but pore diameter decreased to 24 ± 3 nm (Fig. 2b). The pore size significantly decreased due to the introduction of NpC generated by the carbonized FA, which contains microporous domains (pores <1 nm). This results in two distinct classes of pores within the sample, the microporous domain of NpC that adds to the porous domain of pSi [32,40]. The morphology and structure of the NpC shows significant changes with varying pyrolysis temperature. At low temperatures (200-500 °C), a highly chaotic structure of amorphous carbon and polyaromatic microdomains comprising hydrogen and oxygen (hetero) atoms forms the basis of the NpC upon pyrolysis of PFA. The microporosity of PFA has been attributed to this chaotic structure. Above 500 °C, the aromatic microdomains grow significantly such that the region occupied by amorphous carbon is consumed, forming a fragile structure and causing the micropores to collapse leading to a decrease in their average pore mouth dimension [43–45]. At 700 °C and beyond, dehydrogenation takes place along with the rearrangement of carbon atoms to form glassy carbon-like structures within pSi [44]. At temperatures between 1500 and 2000 °C, the polymer precursor completely breaks down forming well-organized graphitic carbon structures, and any structural defects are eliminated. This graphitization process enhances the material density and shrinks the pores. The introduction of such carbon coating stabilizes the pSi surface. The chemical stability provided by this carbonization technique has been well investigated by Tsang and colleagues [46]. By comparing the stability of PFA-pSi in aqueous solution (phosphate-buffered saline,

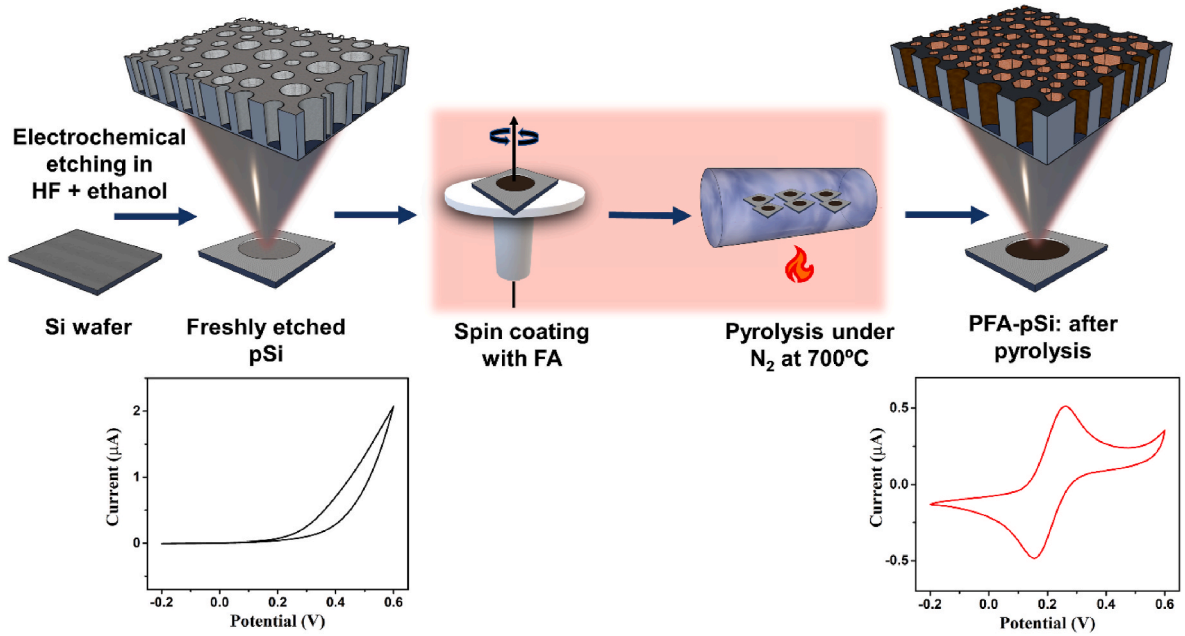

Fig. 1. Schematic of stepwise fabrication and modification of freshly etched pSi using FA, followed by its carbonization.

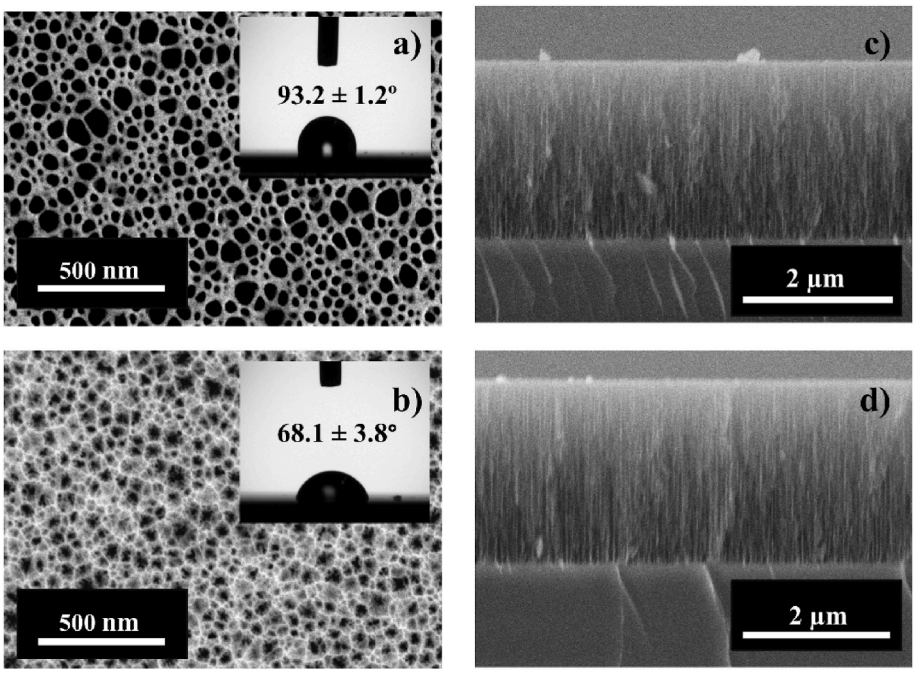

Fig. 2. Top FESEM images and water contact angle photographs (insets) of a) freshly etched pSi and b) PFA-pSi. Cross-sectional FESEM images of c) freshly etched pSi and d) PFA-pSi.

PBS) at pH 7.4 and 12, with pSi modified via three strategies commonly applied to stabilize freshly etched pSi, thermal oxidation at 800 °C, thermal hydrocarbonization (with acetylene, at 700 °C), and hydrosilylation (with undecylenic acid), PFA-pSi showed the highest stability in both neutral and alkaline aqueous solutions [46].

Unlike the ease of tuning of the pore morphology intrinsic of the pSi structure by simply changing the etching parameters, the size of the pores in PFA-pSi can only be tailored to some extent by changing the FA spin-coating conditions: angular velocity (ω) and time. The effect of the applied ω on PFA-pSi pore size was studied with samples prepared from freshly etched pSi featuring an average pore diameter of 60 ± 18 nm, upon PFA modification by spin coating a 20 % ethanolic solution of FA. Three spin-coating conditions were employed, where the ω of the FA infiltration step was set at 400, 1000 or 3000 rpm, keeping the ω of the second step fixed to 4000 rpm (Table S-1, Supplementary Information). The lowest ω gave the smallest pore size, with an average pore size of 20 ± 6 nm, while the highest ω led to the largest pores, with an average size of 36 ± 8 nm.

To further understand the contribution of the ω of FA spin coating toward PFA-pSi pore morphology, the carbon film thickness was studied using spectroscopic ellipsometry (SE) [47]. SE measurements were performed using PFA pyrolyzed on a flat Si surface. SE results showed the effect of ω on the carbon film thickness, providing significantly thicker films at low ω compared to the thickness of films obtained at high ω, *i.e.*, at 400 rpm, 1000 rpm and 3000 rpm film thickness were 49 nm, 31 nm and 26 nm, respectively. This confirms the direct relation between carbon film thickness and PFA-pSi pore size, with thinner films resulting in slightly larger PFA-pSi pores. Please note that while higher ω (>4000 rpm) can be applied, the penetration depth of the carbonized polymeric film would be limited due to the narrow aspect ratio of pSi.

To study the effect of the pyrolyzed PFA coating on the pSi morphology, reflective interferometric Fourier transform spectroscopy (RIFTS) was performed. Results were compared to those obtained for a freshly etched pSi sample. Fig. 3a displays the reflectance spectra for

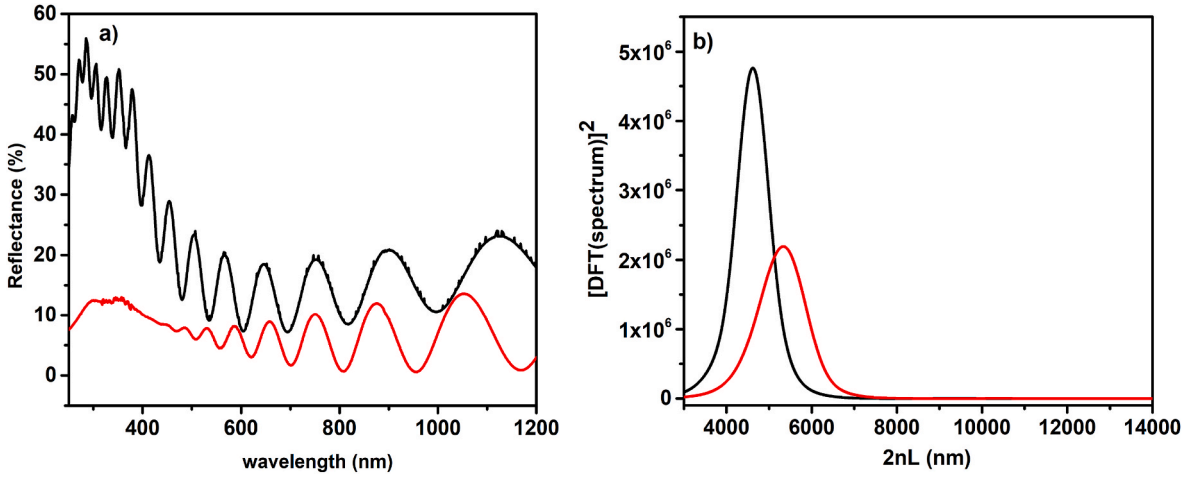

Fig. 3. a) Interferometric reflectance spectra and b) Fourier transformed reflectance spectra for freshly etched pSi (black lines) and PFA-pSi (red lines). (For interpretation of the references to colour in this figure legend, the reader is referred to the Web version of this article.)

both freshly etched pSi and PFA-pSi (prepared after spin coating FA at ω = 1000 rpm), the latter showing a significantly reduced percentage of reflectance. This is due to the increased absorbance of light of the carbon film formed after PFA pyrolysis, an effect that directly depends on the film thickness [46]. The reflectance spectra depict a series of interference fringes, referred to as Fabry-Pérot fringes, that correspond to constructive and destructive interferences when light is reflected from the interfaces of pSi (*i.e.*, pSi-medium and pSi-crystalline Si) [22]. The wavelength of the fringe maxima is given by the following equation:

$$m\lambda_{max} = 2nL \quad (1)$$

where m is the integer correlating the spectral order of the fringe, λ_{max} (nm) is the maximum wavelength of the fringe, n is the refractive index of the pSi layer and L (nm) is the thickness of the pSi layer. The factor *2* represents the optical path taken by the light source where the light source and the detector are at normal incidence [48]. The term *2nL* is often described as the optical path length, also known as EOT. Here, the EOT values for both PFA-pSi and freshly etched pSi were calculated. Fourier transforms were applied to the reflectance spectra of freshly etched pSi and PFA-pSi, providing FFT peaks at 5334 nm and 4918 nm, respectively (Fig. 3b). Using their optical thickness, the refractive indexes (n) of pSi and PFA-pSi were calculated, being 1.07 and 1.21, respectively. These values were used to apply the Bruggeman effective medium approximation [49], which yielded porosity values of 83 ± 1 % and 54 ± 1 % for freshly etched pSi and PFA-pSi, respectively. The change in porosity confirms that the porous structure was partly filled by the pyrolyzed PFA film.

3.1.2. Chemical characterization

The surface properties of PFA-pSi were studied by measuring its wettability using an optical tensiometer. As shown in the inset of Fig. 2b, the PFA-pSi surface was moderately hydrophilic, with a water contact angle of 68 ± 4° when compared to the higher contact angle of freshly etched pSi at 93 ± 1°. The surface properties of carbonized pSi are strongly dependent on the treatment temperature and carbon source. Evidence for changing surface properties has been reported previously. For instance, Tsang *et al.* reported that the carbonaceous pSi formed using PFA when annealed at 700 °C, was fairly hydrophilic with a contact angle of 58 ± 1° [50]. Apart from PFA-pSi, the wettability of THC-pSi and TC-pSi has also been studied in detail. THC-pSi formed when treated at 525 °C retains the hydrophobic nature of freshly etched pSi (122 ± 4°), whereas TC-pSi formed at 800 °C leads to a hydrophilic surface (31 ± 4°) [19,20].

The hydrophilic nature of PFA-pSi is advantageous for infiltrating the porous structure with a wide range of chemicals to introduce the functionalities required for the covalent immobilization of diverse biomolecules used as bioreceptors.

Furthermore, the chemical composition of pSi before and after PFA coating and subsequent pyrolysis was characterized using FTIR. As shown in Fig. 4a (black line), freshly etched pSi displays bands

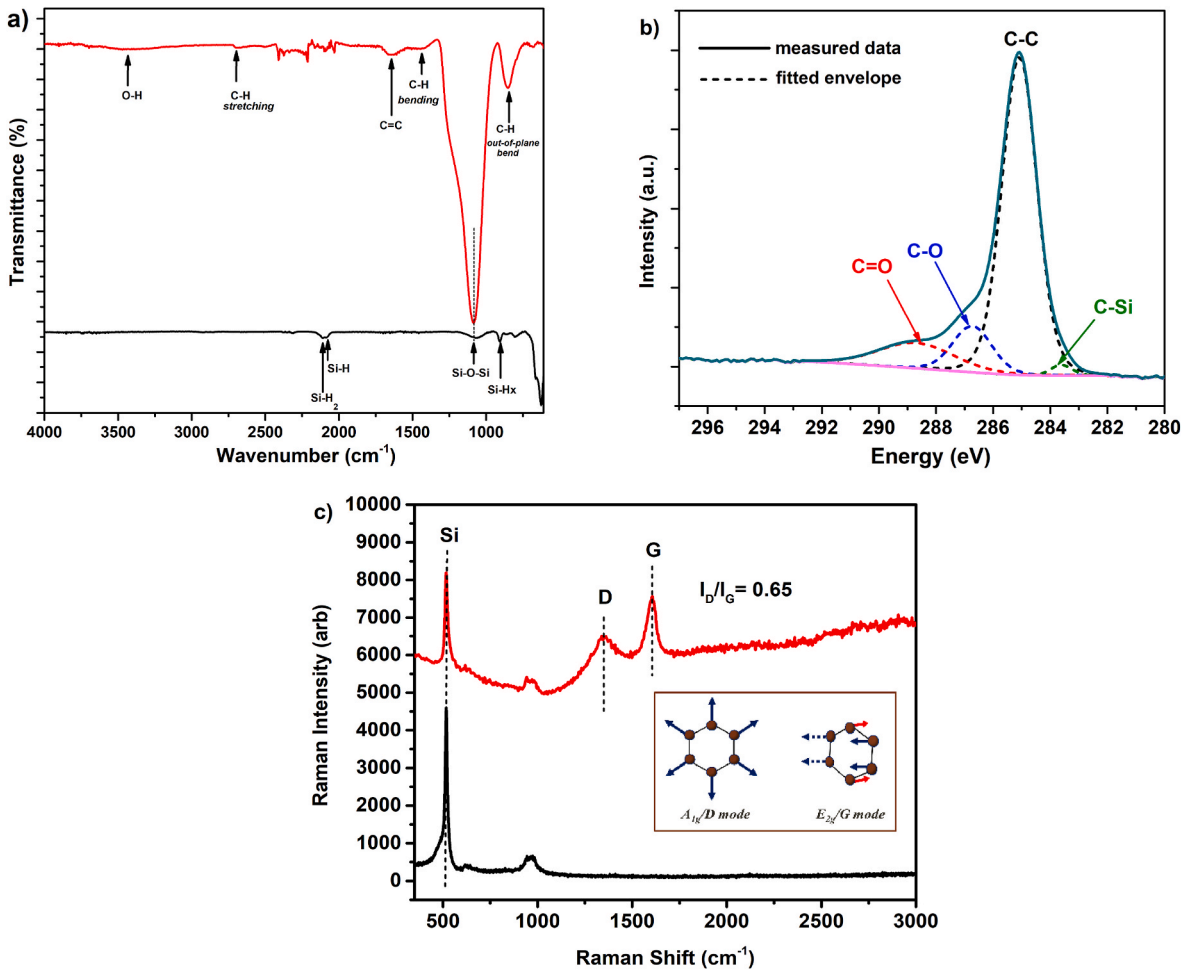

Fig. 4. a) FTIR spectra for freshly etched pSi (black line) and PFA-pSi pyrolyzed at 700 °C (red line), b) C1s XPS spectrum of PFA-pSi (with both measured data and fitted envelope), and c) Raman spectra of freshly etched pSi (black line) and PFA-pSi (red line). The peaks at ~1340 and ~1600 cm^{-1} in the Raman spectra are attributed to the D and G bands of carbon. The intensity ratio of the D and G bands (I_D/I_G) was calculated by Lorentz fitting of the data. Inset in c) showing different modes of vibrations in sp2 C–C bonding. (For interpretation of the references to colour in this figure legend, the reader is referred to the Web version of this article.)

characteristic of Si–H and Si–H_2 stretching vibrations at 2088 and 2110 cm^{-1} along with a bending Si–H mode at 905 cm^{-1}. In addition, another characteristic band for pSi corresponding to the asymmetrical Si–O–Si stretching, is observed at 1050 cm^{-1} [41]. Fig. 4a (red line) shows that the Si–H_x moieties disappeared after polymerization of the deposited FA indicating chemical coverage of the pSi surface. The disappearance of the Si–H is due to the nucleophilic attack on the hydrides by the oxygen atom of the hydroxyl group (OH) featured by PFA. A proposed mechanism based on the one reported by Cleland *et al.* is shown in Fig. S-1 (Supplementary Information) [51]. It is important to highlight the complexity of the polymerization process of FA, recently studied in detail by D'Amico *et al.* [52] and Tondi *et al.* [53]. FA polymerization comprises diverse cross-linking mechanisms that can lead to different chemical structural arrangements such as 1) linear arrangements through methylene and di-methylene ether bridges, 2) ring-opening arrangements to form α,β di-ketones and γ lactones, 3) conjugated structures, and 4) Diels-Alder arrangements between the conjugated and unconjugated chains [53]. Burket *et al.* identified in the FTIR spectrum of PFA, the presence of vibrational modes for some of these structures, mainly the ring-opening structures of furan and the conjugated structures of polymer backbone, prior to carbonization [54]. They reported that after polymerization at 100 °C, the FTIR spectrum of PFA showed a very broad OH stretching vibration at 3400 cm^{-1} along with a strong peak at 3100 cm^{-1} arising from the CH in aromatic rings. Additionally, bands due to carbonyl groups arising from the acid-catalyzed ring opening and 2,5-di-substitution of furan rings were observed at 1710 cm^{-1} and 760 cm^{-1}, respectively [54]. Herein, at pyrolysis temperatures above 500 °C most of the polymer converts to carbon, mainly arising from the polyaromatic domain. Indeed, in Fig. 4a (red line), between 800 and 920 cm^{-1}, a sharp band is observed which can be attributed to CH_2 out-of-plane rocking vibration [53,55]. Further, CH stretching and asymmetric CH_2 bending vibrations are observed at 1419 cm^{-1} and 2715 cm^{-1}, respectively [53,55–57], and a polyaromatic carbon double bond stretching band appears at 1640 cm^{-1}. The spectrum does not show characteristic furan ring vibrations between 1040 and 1100 cm^{-1}, indicating furan rupture. However, the presence of a weak broad OH-stretching band near 3400 cm^{-1} could be associated with FA still present due to incomplete polymerization [54,52,53]. The PFA-pSi surface was also characterized by XPS. Table S–2 (Supplementary Information) presents the elemental analysis on PFA-pSi with their relevant experimental atomic percentages (at%). The XPS C1s spectrum in Fig. 4b shows the absorbance peaks for different carbon functionalities at 283.6 eV (C–Si), 285.1 eV (C–C), 286.7 eV (C–O) and 288.8 eV (C═O). The carbon content in PFA-pSi is mainly attributed to hydrocarbons (73.9 %), with a significantly lower contribution from C═O (12.7 %), C–O (11.9 %) and C–Si species (1.5 %).

Raman spectroscopy was performed to study the properties of the pyrolytic carbon introduced on the pSi surface. The pyrolysis of PFA involves three critical temperatures namely carbonization at 400 °C, followed by nucleation of pyrolytic graphite at 550 °C, and finally, the growth of microcrystalline carbon particles at 700 °C referred to as crystal growth temperature (T_G) [58]. When the temperature reaches T_G, a large number of microcrystallites of pyrolytic graphite are expected to be formed along with the disappearance of PFA degradation compounds, as previously reported by Li *et al.* [58–60]. The Raman spectrum of single-crystalline graphite exhibits two active vibrational modes mainly at 42 cm^{-1} and 1580 cm^{-1} (E_{2g} mode), the latter commonly known as the G band. The Raman spectrum of microcrystallites with disordered carbon shows a broader G band that can blue shift to 1600 cm^{-1}, and a new active vibrational mode at 1350 cm^{-1} (A_{1g} mode), known as the D band [60]. Unlike freshly etched pSi (Fig. 4c, black line), the Raman spectrum of PFA-pSi shows two active vibrational modes at 1350 cm^{-1} (D band) and 1600 cm^{-1} (G band), thereby indicating the presence of microstructured carbon compounds (Fig. 4c, red line). The D band is associated to out-of-plane vibrations attributed to the presence of structural defects at the edge of the crystallites causing a change in carbon symmetry from D_{6h} to C_{3v} [58,61]. Whereas the G band corresponds to in-plane vibrations of sp^2-bonded carbon atoms in graphite crystallites. To assess the disorder level of the pyrolytic carbon on the surface of pSi, the peak intensity ratio of D and G bands (I_D/I_G) was calculated. First, the Raman spectrum for PFA-pSi was baseline subtracted and fitted with the Lorentz function to calculate I_D and I_G. The Lorentz function is a singly peak function expressed as:

$$y = y_0 + \frac{2A}{\pi}\frac{W}{4(X - X_c)^2 + W^2} \quad (2)$$

where A is the peak area, y_0 is the offset, X_C is the centre and W is the full width at half maximum (FWHM). The deconvoluted D and G bands using Lorentz fitting are shown in Fig. S-1 (Supplementary Information). Using this fitting, the I_D/I_G was determined to be 0.65, with an FWHM of 112.2 and 51.7 for the D and G bands, respectively. Although the carbon formed by PFA pyrolysis is ordered and crystalline, the degree of crystallinity is lower compared to graphite. This can be due to the nature of PFA, which basically belongs to a class of polymers that form non-graphitizing carbon upon pyrolysis and hence partly retain amorphous carbon even at high temperature [62]. Fig. 4c shows a characteristic Si lattice mode at 515 cm^{-1}, observed in both pSi [63] and PFA-pSi spectra, confirming that the crystallinity of Si is maintained even after pyrolysis.

3.2. Electrochemical characterization of PFA-pSi

As discussed earlier, PFA pyrolyzed at high temperatures shows excellent conductivity, due to the increase in the transport of charge carriers across the pyrolytic carbon. Owing to this property, here the performance of PFA-pSi (pSi samples etched for 100 s with an average pore diameter of 60 ± 18 nm and a layer thickness of 2.3 ± 0.3 μm; subsequently spin coated with FA at ω = 1000 rpm) as electrochemical transducer is studied extensively through CV and EIS. CV and EIS are powerful and versatile electroanalytical techniques to evaluate the performance of electrodes. CV and EIS measurements were performed in a 2 mM ferrocyanide and 2 mM ferricyanide solution ($[Fe(CN)_6]^{3-/-}$) prepared in 10 mM PBS buffer at pH 7.4. $[Fe(CN)_6]^{3-/-}$ is an anionic inner-sphere redox pair, where the electron transfer rate constant is sensitive to surface carbon. This redox pair behaves as an ideal quasi-reversible system on carbon electrodes [64,65].

3.2.1. Stability, repeatability, and reproducibility

First, CV was used to assess electrode stability, response repeatability and reproducibility among electrodes. Fig. 5a compares the voltammetric response of PFA-pSi and freshly etched pSi. Bare pSi showed poor electrochemical performance with no oxidation (I_{ox}) and reduction (I_{red}) current peaks, whereas PFA-pSi showed a very stable and quasi-reversible response to $[Fe(CN)_6]^{3-/4-}$, proving that surface stabilization is crucial to improve the electrical properties. The repeatability of the electrodes is strongly supported by the results shown in Fig. 5b, corresponding to 20 consecutive cyclic voltammograms. The relative standard deviation (RSD) values associated to the I_{ox} (438 μA) and I_{red} (442 μA) calculated from those consecutive cyclic voltammograms were 1.2 % and 0.4 %, respectively. These values underline the notable response repeatability of PFA-pSi. Furthermore, the reproducibility among PFA-pSi electrodes was evaluated. Fig. S-2 (Supplementary Information) displayed cyclic voltammograms corresponding to the 19th scan obtained using four different PFA-pSi electrodes. RSD values of the I_{ox} and I_{red} calculated for all samples were 3.0 % and 1.7 %, respectively. This underpins the excellent reproducibility among PFA-pSi electrodes, thus further promoting that these platforms can be utilized as a highly capable electrochemical transducer.

3.2.2. Electrochemical potential window of PFA-pSi

The potential of porous carbon electrodes as suitable electrochemical transducers has been exploited owing to their large electrode surface

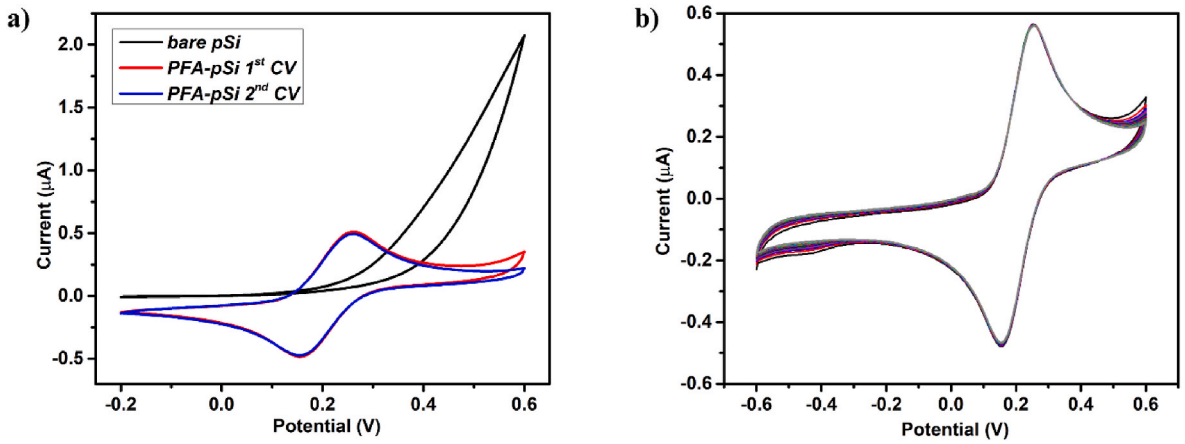

Fig. 5. (a) 1st cyclic voltammogram using bare pSi, and 1st and 2nd scans using PFA-pSi, (b) 20 consecutive cyclic voltammograms using PFA-pSi as working electrode. All measurements were performed in a 2 mM $[Fe(CN)_6]^{3-/4-}$ solution in 10 mM PBS at pH 7.4.

area with enhancement in charge transfer kinetics, leading to higher peak currents and slimming down reaction overpotentials [66]. Porous carbon electrodes such as those based on functionalized graphene sheets (FGS), demonstrated that minute amounts of porosity can significantly increase the apparent electrode kinetics [67]. However, the potential window within that they provide a stable electrochemical response is largely limited to −0.6 V for cathodic and 0.6 V for anodic processes[20, 67]. Here, to estimate the electrochemical working potential window, PFA-pSi was tested by sweeping the applied potential in a window that spanned from −1.5 V to 1.0 V. To that purpose, the electrodes immersed in 10 mM PBS at pH 7.4 were scanned four times within that potential window at a scan rate of 100 mV s^{-1}, followed by their characterization via CV in a 2 mM $[Fe(CN)_6]^{3-/4-}$ solution in a narrower potential range. The objective was to verify that the response to $[Fe(CN)_6]^{3-/4-}$ remained consistent, indicating that the electrode surface remained intact when subjected to high potentials. Results in Fig. 6 prove PFA-pSi is highly stable at very low cathodic potentials (down to −1.5 V) and high anodic potentials (up to 1.0 V). The broad potential window for PFA-pSi underlines the potential for chemosensing applications [33].

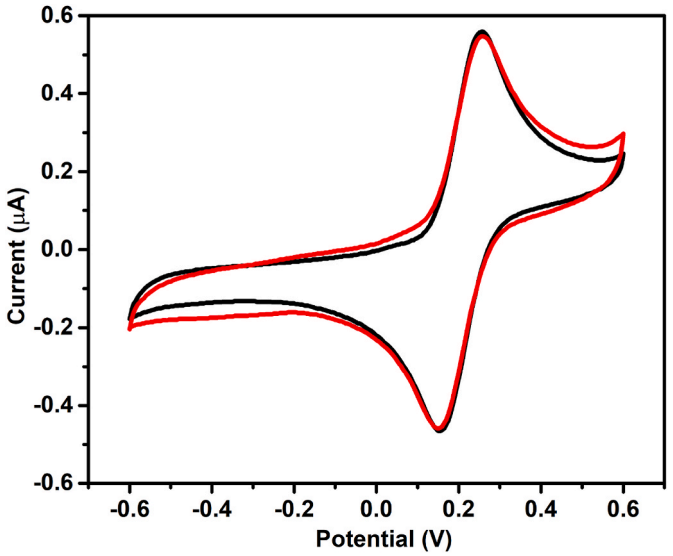

Fig. 6. Cyclic voltammograms of PFA-pSi electrode when measured in a 2 mM $[Fe(CN)_6]^{3-/4-}$ before (black) and after (red) being subjected to four cyclic voltammograms from −1.5 to 1.0 V in PBS. (For interpretation of the references to colour in this figure legend, the reader is referred to the Web version of this article.)

3.2.3. *Comparison of the electrochemical performance of PFA-pSi to that of other carbon-based electrodes*

The overall electrochemical performance of the PFA-pSi electrode was benchmarked against SPCEs and GCEs due to their wide application in electrochemical sensing. In parallel, a relative comparison of the electrochemical performance of PFA-pSi and two other carbon-stabilized pSi electrodes previously reported by Guo *et al.* was also performed (*viz.* THC-pSi and TC-pSi, formed by thermally decomposing acetylene at 525 °C and 800 °C, respectively) [20]. To compare the electrochemical performance of these electrodes, first, the electroactive surface area was calculated, a critical factor given its direct effect on the electrode signal [68].

CV data against $[Fe(CN)_6]^{3-/-}$ was used to estimate the electroactive surface area of PFA-pSi using the Randles-Ševčík equation (see note 1 in the Supplementary Information), and the calculated value was compared to the results obtained using conventional flat electrodes, such as SPCE and GCE, along with THC-pSi and TC-pSi electrodes. The electroactive surface area of the PFA-pSi electrode when normalized to their geometric area was 2- and 1.5 times larger than that of SPCE and GCE, respectively (Table 1). Moreover, thanks to the morphological versatility of PFA-pSi, its effective surface area can be easily altered by tuning pore size and thickness and hence can be adopted for different sensing applications. This gives PFA-pSi, but also THC-pSi and TC-pSi, an added advantage over conventional flat electrodes in their ability to improve the sensitivity of the electrode by just adjusting the fabrication parameters.

To further compare the electrochemical performance of PFA-pSi against commercial electrodes, and other carbon-stabilized pSi samples, voltammetric results were analyzed from which the important parameters are also summarized in Table 1, including I_{ox} and I_{red} (normalized by the geometric surface area), peak-to-peak potential separation (ΔE_p), and half-wave potential ($E_{1/2}$) values. Results show that PFA-pSi, similar to THC-pSi and TC-pSi, clearly outperformed SPCE and GCE, with very large peak current values. Such signal enhancement is attributed to the large electroactive surface area featured by all carbon-stabilized pSi samples, which can be tuned according to the measuring requirements. The ΔE_p values shown by PFA-pSi are smaller than those for SPCE and similar to those for GCE, indicating a rather rapid electron transfer. Nonetheless, previously reported ΔE_p values for THC-pSi and TC-pSi (58 mV and 66 mV, respectively) are closer to the expected ΔE_p value (59 mV) for a reversible one-electron transfer reaction obtained from the Nernst equation [20]. The larger ΔE_p for PFA-pSi (105 mV) relative to that of both THC-pSi and TC-pSi indicates the system is quasi-reversible [69]. To deepen into the PFA-pSi properties driving the electron transfer reaction, its kinetics was assessed.

The nature of a heterogeneous electrochemical reaction either

Table 1
Electroactive, geometric, normalized surface area and electrochemical performance showcasing normalized I_{ox} and I_{red}, peak current ratio (I_{red}/I_{ox}), ΔE_p, and half-wave potential ($E_{1/2}$), of PFA-pSi, THC-pSi, TC-pSi, SPCE and GCE extracted from cyclic voltammograms measured in 2 mM $[Fe(CN)_6]^{3-/4-}$ solution in 10 mM PBS at pH 7.4.

Electrodes	Electroactive surface area (cm^2)	Geometric surface area (cm^2)	Normalized surface area [a]	Normalized I_{ox} (μA cm^{-2})	Normalized I_{red} (μA cm^{-2})	I_{red}/I_{ox}	ΔE_p (mV)	$E_{1/2}$ (mV)
PFA-pSi	0.669 ± 0.002	0.442 ± 0.001	1.52 ± 0.02	991	−1000	1.0	105	168
THC-pSi [b]	0.588 ± 0.002	0.442 ± 0.001	1.33 ± 0.02	778	−563	0.7	58	208
TC-pSi [b]	0.770 ± 0.001	0.442 ± 0.001	1.74 ± 0.01	975	−774	0.8	66	210
SPCE [b]	0.117 ± 0.001	0.126 ± 0.001	0.93 ± 0.03	492	−516	1.0	213	117
GCE [b]	0.074 ± 0.002	0.071 ± 0.001	1.04 ± 0.02	746	−634	0.9	86	185

[a] Normalized surface area = electroactive surface area/geometric surface area.
[b] Values taken from Guo *et al.* for comparison [20].

reversible, quasi-reversible, or irreversible is fairly determined by the rate at which the electron transfer occurs between the working electrode surface and the electroactive species in solution [69]. It is therefore important to estimate the heterogeneous electron transfer rate constant (k_0) to comprehend the speed of electron transfer between the electrode surface and an electroactive species, thus shedding more insight into the kinetics and performance of the electrochemical transducer [70]. For long, the method developed by Nicholson using the ΔE_p as a function of the ν set to measure the corresponding cyclic voltammograms was adopted by electrochemists to calculate k_0, which was subsequently modified by Lavagnini and coworkers (see note 2 in the Supplementary Information) [71,72].

Using the Nicholson–Lavagnini equation, the value of k_0 for PFA-pSi was calculated to be 7.4×10^{-3} cm s^{-1}, thus supporting faster electron transfer when compared to the k_0 value of 3.6×10^{-4} cm s^{-1} estimated by Lavagnini *et al.* for a carbon paste electrode under the same working conditions [73]. The excellent electrochemical performance of PFA-pSi is further supported by its electron transfer kinetics (Table 2).

Under the same conditions, the k_0 value for PFA-pSi was close to those of SPCE and GCE, but significantly lower than those of THC-pSi and TC-pSi. The differences in kinetics when compared to THC-pSi and TC-pSi can be attributed to the surface carbon microstructure arising from the different carbon sources for the thermal carbonization procedure. Acetylene, being a gaseous carbon source, shows high physisorption onto the pSi surface, thus resulting in a coating of Si–C and Si–O–C structures [74]. While FA is initially a solubilized carbon source that undergoes a complex polymerization mechanism, and eventually forms pyrolytic carbon when heated at high temperature. Moreover, as a result of the higher annealing temperature, the amount of sp^2 hybridized carbon and π electrons present is relatively higher in case of platforms carbonized with acetylene (such as TC-pSi) when compared to the ones modified with PFA. When using $[Fe(CN)_6]^{3-/-}$ as redox pair, the disorder in carbon surface structure can significantly impact kinetics as k_0 is sensitive to specific surface reactive sites present at defects [75]. In such case, Raman spectroscopy as previously shown can be used to recognize possible structural defects. Besides PFA-pSi, THC-pSi and TC-pSi also present microstructured carbon compounds with structural defects, as confirmed by the presence of the D band [76]. The intensity ratio of the D and G bands (I_D/I_G) estimates the defects on carbon samples, where higher ratio indicates more defects [77]. In case of THC-pSi (I_D/I_G = 0.72) and TC-pSi (I_D/I_G = 0.95) [76], the intensity is significantly higher compared to PFA-pSi (I_D/I_G = 0.65), thereby explaining a possible reason to the faster kinetics observed for THC-pSi and TC-pSi. Apart from structural defects, the surface of these three carbon-stabilized pSi platforms was further analyzed using XPS to deepen into their surface oxides. Fig. S-3 (Supplementary Information) shows the XPS spectra for the three pSi platforms with PFA-pSi depicting relatively higher surface oxides in comparison to THC-pSi and TC-pSi platforms. Therefore, PFA-pSi adds to the list of carbon-stabilized pSi nanostructures with great potential as effective Faradaic electrochemical platforms, with the added value of broadening the range of surface carbon microstructures and chemical functionalities.

To complete the electrochemical characterization of PFA-pSi and its comparison against SPCE, GCE, THC-pSi and TC-pSi, EIS measurements were recorded, and the obtained Nyquist plots were fitted to the Randles circuit shown in the inset of Fig. 7. The Randles circuit corresponds to the more basic equivalent electrical circuit involving the charge transfer resistance (R_{ct}), the resistance of the solution (R_s) which is associated with the electrochemical kinetics, the Warburg impedance (W), and the double-layer capacitance (C_{dl}). Table 3 summarizes the results obtained for PFA-pSi after fitting the Nyquist plot to the Randles circuit, and compares those results to those previously reported for THC-pSi and TC-pSi, and commercial electrode such as SPCE and GCE. As expected, due to the larger surface-to-volume ratio of the three nanostructured porous electrodes, their R_{ct} values were much lower than those of SPCE (747 ± 33 Ω) and GCE (244 ± 8 Ω). Also, amongst the carbon-stabilized porous electrodes, the PFA-pSi platform showed a considerably lower R_{ct} (11.4 ± 0.5 Ω), 2.3- and 4.7-fold lower than R_{ct} values associated to THC-pSi and TC-pSi electrodes, respectively. In addition, the reproducibility in EIS measurements performed using PFA-pSi, calculated as the RSD of the R_{ct} (shown in Fig. 6, with n = 4), was evaluated. The RSD value of 4.7 %

Table 2
k_0 values for PFA-pSi, THC-pSi, TC-pSi, SPCE and GCE using a 2 mM $[Fe(CN)_6]^{3-/4-}$ solution in 10 mM PBS at pH 7.4.

Electrodes	k_0 (cm s^{-1})	Nature of electrochemical reaction
PFA-pSi	7.4×10^{-3}	Quasi-reversible
THC-pSi	2.4	Reversible
TC-pSi	0.1	Reversible
SPCE	1.0×10^{-3}	Quasi-reversible
GCE	1.1×10^{-4}	Quasi-reversible

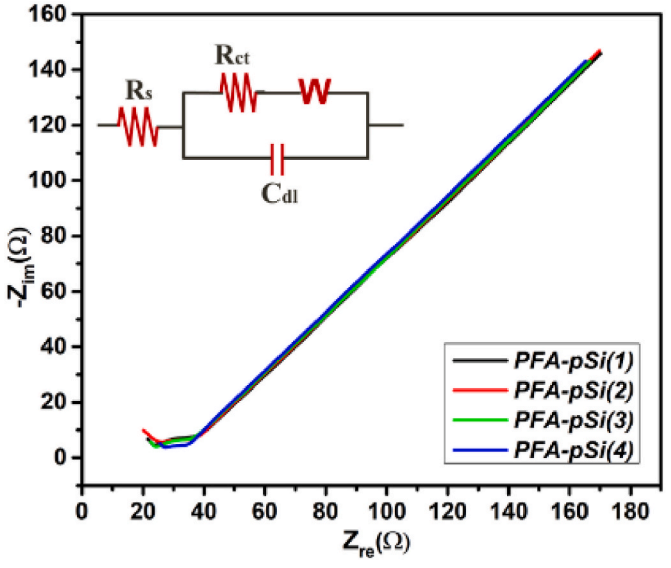

Fig. 7. Nyquist plots of PFA-pSi samples when performing EIS measurements in a 2 mM $[Fe(CN)_6]^{3-/4-}$ solution (n = 4).

Table 3
Solution resistance (Rs), charge-transfer resistance (Rct) obtained from EIS for four electrodes *viz.* PFA-pSi, THC-pSi, TC-pSi, SPCE and GCE when measured in a 2 mM $[Fe(CN)_6]^{3-/4-}$ solution.

Electrode	R_s (Ω)	R_{ct} (Ω)	C_{dl} (nF)
PFA-pSi	17 ± 1	11 ± 1	316 ± 8
THC-pSi[a]	74 ± 2	26 ± 2	75 ± 4
TC-pSi[a]	75 ± 2	54 ± 1	72 ± 3
SPCE[a]	75 ± 6	747 ± 33	937 ± 59
GCE[a]	166 ± 9	244 ± 8	1247 ± 65

[a] Values taken from Guo *et al.* for comparison [20].

was within the range of the RSD values previously obtained for THC-pSi and TC-pSi, 6.2 % and 2.4 %, respectively [20], confirming the excellent reproducibility of the EIS response of these carbon-stabilized pSi electrodes. Apart from the R_{ct}, the electric capacitance owing to the electric double layer formed at the interface between an electrode and its surrounding electrolyte was also studied. It plays a decisive role in understanding the signal-to-noise ratio of a sensor thereby interpreting its sensitivity [20,78]. Although a porous electrode is known to enhance mass transport rate by providing a large surface area, large C_{dl} values can significantly impact the electrochemical readout [79,80]. Importantly, the C_{dl} values for PFA-pSi (316 ± 8 nF) were relatively lower than those of conventional electrodes such as GCE (1247 ± 65 nF) and SPCE (937 ± 59 nF) [20]. Thus, showcasing no significant negative effect on signal-to-noise ratio. These results support the efficiency of PFA-pSi as electrochemical transducer, widening the choice of suitable carbon-stabilized electrodes *viz.* THC-pSi and TC-pSi electrodes, to design chemosensors and biosensors.

3.2.4. *Electrochemical behavior of PFA-pSi towards different redox species*

To understand the effect of the structural and chemical nature of PFA-pSi on its electrochemical performance, its CV response against three redox species with different electrode kinetics was compared. Along with $[Fe(CN)_6]^{3-/-}$, hexamine ruthenium ($[Ru(NH_3)_6]^{2+/3+}$, a cationic outer-sphere redox species), and hydroquinone (HQ, a proton sensitive neutral aromatic compound) were used to analyze the electrochemical behavior of PFA-pSi (Fig. 8). All three redox species were prepared in 10 mM PBS (pH 7.4) at a concentration of 2 mM. The kinetics of $[Ru(NH_3)_6]^{2+/3+}$ is neither sensitive to surface structure or

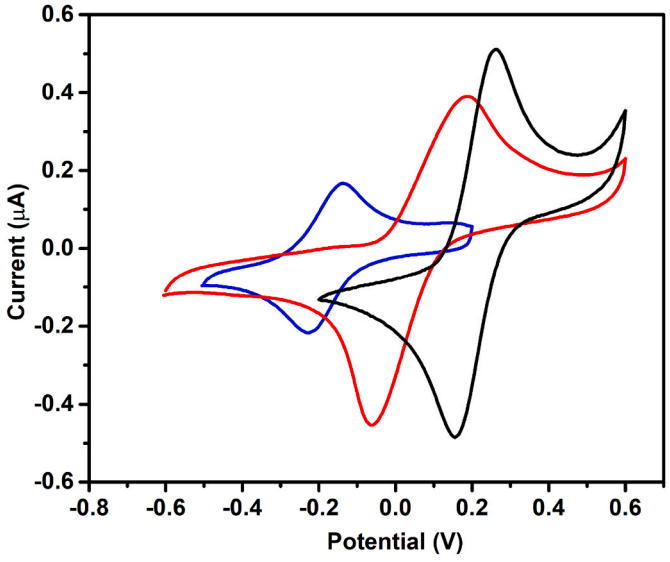

Fig. 8. Cyclic voltammograms of PFA-pSi sample when measured in a 2 mM mM $Ru[(NH_3)_6]^{2+/3+}$(blue line), HQ (red line) and $[Fe(CN)_6]^{3-/-}$(black line) solutions in 10 mM PBS at pH 7.4. (For interpretation of the references to colour in this figure legend, the reader is referred to the Web version of this article.)

oxide functionality, but to the density of electronic states [20,65,81]. HQ is proton sensitive, and thus its kinetics is significantly governed by reactions involving proton carriers [82]. The ΔE_p values for the three redox species obtained from Fig. 8 are summarized in Table S-3 (Supplementary Information). ΔE_p values for PFA-pSi using $Ru[(NH_3)_6]^{2+/3+}$ and HQ turn out to be 88 mV and 255 mV, respectively, which are similar to those shown by a GCE (70 mV for $Ru[(NH_3)_6]^{2+/3+}$ and 282 mV for HQ, as shown in Tables S–3). To further support the similarities in the electrochemical performance of PFA-pSi and GCE, C1s XPS spectra of both electrodes were compared. Previous reports showed prominent absorbance peaks at 284.5 eV (C–C), 286.3 eV (C–O) and 287.7 eV (C═O) in the C1s XPS spectrum of GCE [83], data that confirm equivalent carbon functionalities to those of PFA-pSi [84]. This shows for the first time that not only the nature of pyrolyzed PFA leads to carbon functionalities similar to those present in glassy carbon [46], but importantly its electrochemical performance closely resembles that of a GCE, while providing additional advantages such as the tunable pore morphology, which can be used to easily increase its active surface area, and its versatile surface chemistry conducive to a diverse range of functionalization strategies.

3.3. *PFA-pSi-based impedimetric DNA sensor*

After fully characterizing the performance of PFA-pSi and showcasing its strength as an electrochemical transducer, its applicability as a biosensing platform was demonstrated by the development of a label-free impedimetric DNA sensor. The surface of PFA-pSi was modified via covalent immobilization of a single stranded DNA (ssDNA) capture probe complementary to a 25 bases sequence of a 16SrRNA gene associated to *Staphylococcus aureus* (*S. aureus*). Sensing takes advantage of the DNA-base pairing interaction between both sequences. DNA was used as target instead of RNA due to the fact that the former is cheaper and is less prone to degradation. DNA can work as a good model system for facile subsequent translation to RNA targets. To exploit the pore morphological features of PFA-pSi, a biosensing mechanism based on the blockage of the pores within the structure caused upon hybridization was selected. The partial blockage of the pores caused mainly from the electrostatic repulsions and steric hindrance upon target hybridization to the ssDNA-modified PFA-pSi, hinders the diffusion of the negatively charged redox species, such as $[Fe(CN)_6]^{3-/4-}$, added to the measuring solution as shown in Fig. 9a. This partial pore blockage can be evaluated in terms of the variation of the parameters calculated from the Randles circuit fitting obtained from the Nyquist plots.

To prepare the biosensor, initially PFA-pSi with an average pore diameter of 24 ± 3 nm and a thickness of 2.3 ± 0.3 μm (prepared using spin-coating conditions consisting of 2 min at 1000 rpm followed by 1 min at 4000 rpm, as depicted in Table S-1, Supplementary Information) was selected to accommodate the immobilized ssDNA capture probe and allow free diffusion of the target. The PFA-pSi surface was first functionalized by grafting hydrazide-phenyl radicals through electrochemical reduction of 4-aminobenzoic hydrazide (4-ABH) [41]. 4-ABH provided the functional groups required for the covalent immobilization of the bioreceptor. Next, the biorecognition element, an amine-modified ssDNA (NH_2-ssDNA) complementary to a 16SrRNA growth factor from *S. aureus*, was immobilized via glutaraldehyde cross-linking. After 4-ABH electrografting, PFA-pSi substrates were incubated with glutaraldehyde that acted as a bifunctional linker between the hydrazide-functionalized electrode and the NH_2-terminated ssDNA probe. The aldehyde group on one end of glutaraldehyde reacted with the hydrazide group to form hydrazone linkages [85], whereas the other end reacted with the amino group on the ssDNA probe to form an imine bond enabling covalent immobilization of the ssDNA probe on the pSi electrode surface.

FTIR was used to confirm the surface modification at each stage of PFA-pSi biosensor development. Fig. S-4 (Supplementary Information) shows the FTIR spectrum of PFA-pSi after 4-ABH electrografting, with a

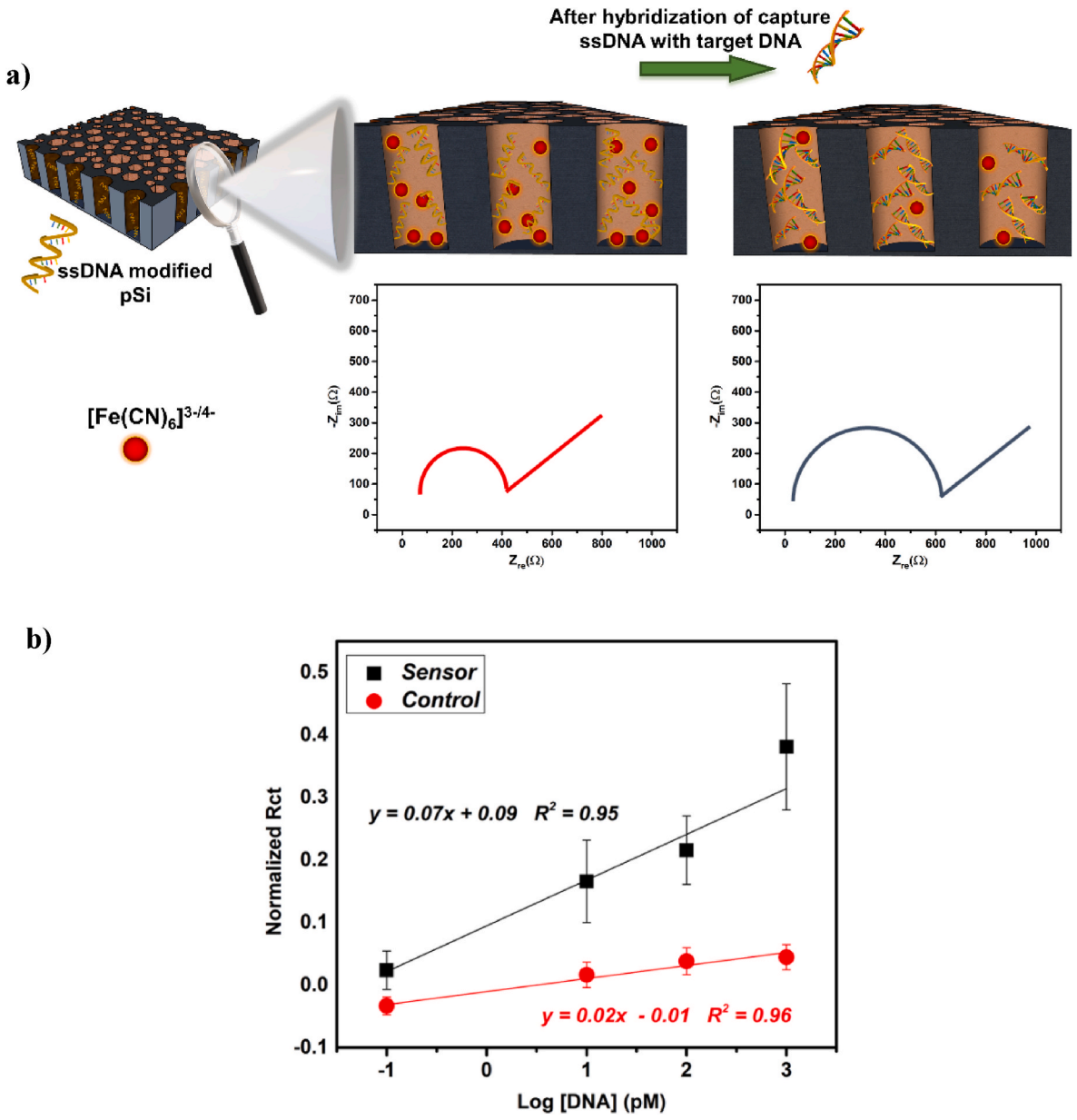

Fig. 9. a) A schematic showcasing pore blockage sensing mechanism for a PFA-pSi-based DNA sensor, and corresponding EIS spectra expected before and after ssDNA hybridization. b) Calibration curves for target ssDNA using PFA-pSi biosensors prepared with complementary ssDNA capture probe (black), and controls prepared with a random ssDNA sequence (red). Impedimetric measurements were performed in a 2 mM $[Fe(CN)_6]^{3-/-}$ solution. Data are shown as mean ± standard error, n = 5. (For interpretation of the references to colour in this figure legend, the reader is referred to the Web version of this article.)

characteristic N–H stretching vibration band around 3410 cm^{-1}. The presence of the hydrazide-phenyl group was confirmed by the band at 1500 cm^{-1}, representing the C–N mode. The carbonyl C═O stretching modes arising from the benzoic hydrazide were displayed in the region of 1650 cm^{-1} in agreement with previous reports 41,42. After glutaraldehyde cross-linking, a CHO band from the aldehyde group was observed at 1700 cm^{-1} [86]. Finally, the FTIR spectrum of the PFA-pSi sample upon covalent immobilization of the ssDNA capture probe showed a band around 1650 cm^{-1} that corresponded to the stretching vibration of the C═N of the imine group. The broad peak at approximately 3413 cm^{-1} could be assigned to the N–H stretch of the amine group from the NH_2-modified ssDNA. Nonetheless, the imine peak confirmed that DNA was successfully immobilized.

In addition to FTIR, electrochemical characterization via EIS was performed to confirm the immobilization of the NH_2-ssDNA capture probe on PFA-pSi. EIS measurements were performed at each step of sensor modification in the presence of 2 mM $[Fe(CN)_6]^{3-/4-}$ solution in 10 mM PBS buffer at pH 7.4. Fig. S-5 (Supplementary Information) showed a significant increase in R_{ct} after 4-ABH grafting on PFA-pSi, with R_{ct} values of 750 ± 84 Ω compared to 14.1 ± 1.8 Ω for the unmodified PFA-pSi. The results also confirmed the successful immobilization of the ssDNA capture probe after 4-ABH functionalization. The increase of R_{ct} to 1077 ± 70 Ω was attributed to the electrostatic repulsion between $[Fe(CN)_6]^{3-/4-}$ species and the negatively charged ssDNA.

For the biosensing step, impedimetric measurements were conducted after incubating the sensor with target ssDNA over a wide range of concentration from 0.1 to 1000 pM. The obtained spectra were fitted to the equivalent Randles circuit (as shown in the inset of Fig. 7), and the response to target ssDNA was evaluated from the variation of the R_{ct} as any interfacial changes occurring at the surface of the electrode strongly affect this circuit element. Changes in the R_{ct} measured before and after

hybridization were normalized as follows:

$$\Delta R_{ct} = (R_{ct^\circ} - R_{ct}) / R_{ct^\circ} \quad (3)$$

where ΔR_{ct} is the normalized change in R_{ct}, and R_{ct° and R_{ct} are the R_{ct} values prior and after incubation in a target ssDNA solution at a given concentration, respectively. We hypothesize that the change in R_{ct} is mainly due to the pore blockage caused by the hybridization event as mentioned earlier leading to the hindrance of the diffusion of $[Fe(CN)_6]^{3-/4-}$ added to the solution [87,88].

Along with the DNA sensor, controls were prepared by immobilizing a random sequence of ssDNA instead of the capture probe. The ΔR_{ct} values calculated for both DNA and control sensors were plotted against the logarithmic concentration of target ssDNA as depicted in Fig. 9b. On the one hand, ΔR_{ct} values for sensors increased linearly with the concentration of target ssDNA. On the other hand, when comparing to the values obtained from controls (p-value of 0.04), it was confirmed that the difference between biosensors and controls was statistically significant. This confirmed that the changes in R_{ct} measured by the developed DNA sensor could be assigned to the hybridization with the complementary target ssDNA. The limit of detection (LOD) was estimated using the equation $y_{LOD.} = y_{blank} + 3S_{blank}$ where y_{blank} represents the normalized R_{ct} in buffer solution whereas S_{blank} is the standard deviation of the replicates (n = 5) [89]. An LOD of 1.4 pM was obtained, underpinning the great potential of this sensing platform to detect tiny concentrations of DNA analytes, as it outperforms the results previously reported by similar DNA sensing platforms based on electrochemically measuring the pore blockage caused upon analyte hybridization [90–93]. All those sensors used nanoporous alumina membranes to build the biorecognition layer, in some cases including signal amplification by enhancing the pore blockage through extending the DNA target via a polymerase reaction [91], or using gold nanoparticles as labels [93]. The dual role of PFA-pSi as biorecognition layer and transducing element is hypothesised to be responsible of the sensitivity enhancement achieved.

4. Conclusion

Successful fabrication and thorough characterization of a novel electrochemical transducer built from *in-situ* carbonization of PFA on pSi is reported. Using FESEM, EP and RIFTS the morphological features of synthesized PFA-pSi were systematically studied. FTIR, Raman spectroscopy and XPS results showed the chemical composition of the carbon film formed and the nature of pyrolytic carbon on the PFA-pSi surface. For the first time, the electrochemical performance of PFA-pSi was explored and compared to that of both carbon-stabilized pSi (*i.e.*, THC-pSi and TC-pSi), and SPCEs and GCEs. Results demonstrate the use of PFA-pSi as a highly suitable electrochemical transducer, owing to its remarkable stability over a potential window wider than that of THC-pSi and TC-pSi, and its excellent electrochemical performance, underpinned by faster electron transfer kinetics and large electroactive surface area. One of the key features that distinguishes PFA-pSi from other conventional electrodes is the combination of the advantages derived from the use of pSi along with the polymerization and carbonization of FA infiltrated within its structure to form a highly conductive carbon layer. Moreover, pyrolyzed PFA has shown a higher I_D/I_G ratio compared to that of graphite, being this ratio correlated with a higher electrical conductivity. Therefore, PFA-pSi does not only provide a large surface area-to-volume ratio, but also the possibility to easily adjust the electroactive surface area by simply changing the pSi anodization conditions and FA spin-coating parameters, adding value to the electrochemical performance of PFA-pSi when compared to that of both SPCEs and GCEs.

Importantly, the electrochemical behavior of PFA-pSi was studied using three redox species namely $[Fe(CN)_6]^{3-/4-}$, Ru $[(NH_3)_6]^{2+/3+}$ and HQ, with results exhibiting better performance compared to GCE, results that were further supported by PFA-pSi XPS characterization showing similar carbon functionalities. To demonstrate the potential of PFA-pSi in biosensing applications, an impedimetric DNA sensor was developed showing a low LOD of 1.4 pM for a DNA analyte used as a model of a 16SrRNA used to identify *S. aureus*, underlining the potential of this new class of carbon-stabilized pSi nanostructures as efficient (bio) sensing systems in future. Specially, we envisage the highest potential of this platform to be in the development of biosensors based on the pore-blockage sensing principle, harnessing other biorecognition elements in addition to oligonucleotides for DNA/RNA sensing.

CRediT authorship contribution statement

Anandapadmanabhan A. Rajendran: Formal analysis, Investigation, Validation, Writing – original draft. **Keying Guo:** Formal analysis, Investigation. **Alberto Alvarez-Fernandez:** Formal analysis, Writing – review & editing. **Thomas R. Gengenbach:** Formal analysis, Investigation. **Marina B. Velasco:** Investigation. **Maximiliano J. Fornerod:** Investigation. **Kandeel Shafique:** Investigation. **Máté Füredi:** Investigation. **Pilar Formentín:** Investigation. **Hedieh Haji-Hashemi:** Investigation. **Stefan Guldin:** Writing – review & editing. **Nicolas H. Voelcker:** Conceptualization, Supervision, Writing – review & editing. **Xavier Cetó:** Conceptualization, Supervision, Writing – review & editing. **Beatriz Prieto-Simón:** Conceptualization, Funding acquisition, Project administration, Supervision, Writing – review & editing.

Declaration of competing interest

The authors declare that they have no known competing financial interests or personal relationships that could have appeared to influence the work reported in this paper.

Data availability

Data will be made available on request.

Acknowledgements

The project is supported by a COFUND project from the European Union's Horizon 2020 research and innovation program under the Marie Sklodowska-Curie grant agreement No.713679 and the Universitat Rovira i Virgili (URV). Authors acknowledge financial support from the ERA-NET ICRAD (International Coordination of Research on Infectious Diseases) and the Spanish State Research Agency (AEI/10.13039/501100011033; PCI2020-120693-2), and from grant PID2021-124867OB-I00 funded by MCIN/AEI/10.13039/501100011033 and by "ERDF A way of making Europe". A.A.F., M.J.F., and S.G. acknowledge funding by an EPSRC New Investigator Award (EP/R035105/1). Special thanks to Dr Laura K. Acosta and Dr Saeed Bahadorikhalili, for helping with optical interference spectroscopy and PFA-pSi sample preparation, respectively.

Appendix A. Supplementary data

Supplementary data to this article can be found online at https://doi.org/10.1016/j.mtadv.2024.100464.

References

[1] M. Zhou, H.L. Wang, S. Guo, Towards high-efficiency nanoelectrocatalysts for oxygen reduction through engineering advanced carbon nanomaterials, Chem. Soc. Rev. 45 (2016) 1273–1307, https://doi.org/10.1039/C5CS00414D.
[2] S. Liu, X. Guo, Carbon nanomaterials field-effect-transistor-based biosensors, NPG Asia Mater. 4 (2012), https://doi.org/10.1038/am.2012.42 e23.
[3] T. Wei, Y. Chen, W. Tu, Y. Lan, Z. Dai, A phosphomolybdic acid anion probe-based label-free, stable and simple electrochemical biosensing platform, Chem. Commun. 50 (2014) 9357–9360, https://doi.org/10.1039/C4CC03555K.
[4] N. Mohamad Nor, N.H. Ramli, H. Poobalan, K. Qi Tan, K. Abdul Razak, Recent advancement in disposable electrode modified with nanomaterials for

electrochemical heavy metal sensors, Crit. Rev. Anal. Chem. 53 (2023) 253–288, https://doi.org/10.1080/10408347.2021.1950521.
[5] X. Yu, B. Munge, V. Patel, G. Jensen, A. Bhirde, J.D. Gong, S.N. Kim, J. Gillespie, J. S. Gutkind, F. Papadimitrakopoulos, J.F. Rusling, Carbon nanotube amplification strategies for highly sensitive immunodetection of cancer biomarkers, J. Am. Chem. Soc. 128 (2006) 11199, https://doi.org/10.1021/JA062117E.
[6] Q. Cao, H. Zhao, Y. Yang, Y. He, N. Ding, J. Wang, Z. Wu, K. Xiang, G. Wang, Electrochemical immunosensor for casein based on gold nanoparticles and poly(L-Arginine)/multi-walled carbon nanotubes composite film functionalized interface, Biosens. Bioelectron. 26 (2011) 3469–3474, https://doi.org/10.1016/J.BIOS.2011.01.027.
[7] S. Eissa, A. Ng, M. Siaj, M. Zourob, Label-free voltammetric aptasensor for the sensitive detection of microcystin-LR using graphene-modified electrodes, Anal. Chem. 86 (2014) 7551–7557, https://doi.org/10.1021/AC501335K.
[8] J. Wang, J. Wen, H. Yan, Recent applications of carbon nanomaterials for microRNA electrochemical sensing, Chem. Asian J. 16 (2021) 114–128, https://doi.org/10.1002/asia.202001260.
[9] Z. Wang, Z. Dai, Carbon nanomaterial-based electrochemical biosensors: an overview, Nanoscale 7 (2015) 6420–6431, https://doi.org/10.1039/c5nr00585j.
[10] J.N. Tiwari, V. Vij, K.C. Kemp, K.S. Kim, Engineered carbon-nanomaterial-based electrochemical sensors for biomolecules, ACS Nano 10 (2016) 46–80, https://doi.org/10.1021/acsnano.5b05690.
[11] K. Scida, P.W. Stege, G. Haby, G.A. Messina, C.D. García, Recent applications of carbon-based nanomaterials in analytical chemistry: critical review, Anal. Chim. Acta 691 (2011) 6–17, https://doi.org/10.1016/j.aca.2011.02.025.
[12] M. Lanza, Y. Wang, T. Gao, A. Bayerl, M. Porti, M. Nafria, Y. Zhou, G. Jing, Y. Zhang, Z. Liu, D. Yu, H. Duan, Electrical and mechanical performance of graphene sheets exposed to oxidative environments, Nano Res. 6 (2013) 485–495, https://doi.org/10.1007/s12274-013-0326-6.
[13] A.J. Saleh Ahammad, J.J. Lee, M.A. Rahman, Electrochemical sensors based on carbon nanotubes, Sensors 9 (2009) 2289, https://doi.org/10.3390/S90402289.
[14] Y. Liang, Y. Xu, Y. Tong, Y. Chen, X. Chen, S. Wu, Graphene-based electrochemical sensor for detection of hepatocellular carcinoma markers, Front. Chem. 10 (2022) 883627, https://doi.org/10.3389/FCHEM.2022.883627.
[15] M. Coroş, S. Pruneanu, R.-I. Stefan-van Staden, Review—recent progress in the graphene-based electrochemical sensors and biosensors, J. Electrochem. Soc. 167 (2020) 037528, https://doi.org/10.1149/2.0282003JES.
[16] Á. Torrinha, T.M.B.F. Oliveira, F.W.P. Ribeiro, S. Morais, A.N. Correia, P. de Lima-Neto, Advantages and limitations of functionalized graphene-based electrochemical sensors for environmental monitoring, Funct. Nanomater.-Based Electrochem. Sens. (2022) 487–520, https://doi.org/10.1016/B978-0-12-823788-5.00009-0.
[17] Peter T. Kissinger, William R. Heineman (Eds.), Laboratory Techniques in Electroanalytical Chemistry, second ed., Marcel Dekker, New York, 1996..
[18] J. Salonen, M. Björkqvist, J. Paski, Temperature-dependent electrical conductivity in thermally carbonized porous silicon, Sens. Actuators A Phys. 116 (2004) 438–441, https://doi.org/10.1016/J.SNA.2004.05.005.
[19] J. Salonen, E. Mäkilä, Thermally carbonized porous silicon and its recent applications, Adv. Mater. 30 (2018) 1703819, https://doi.org/10.1002/ADMA.201703819.
[20] K. Guo, A. Sharma, R. Jun Toh, E. Alvárez de Eulate, T.R. Gengenbach, X. Cetó, N. H. Voelcker, B. Prieto-Simón, K. Guo, N.H. Voelcker, B. Prieto-Simón, A. Sharma, E. Alvárez de Eulate, X. Cetó, R.J. Toh, T.R. Gengenbach, Porous silicon nanostructures as effective faradaic electrochemical sensing platforms, Adv. Funct. Mater. 29 (2019) 1809206, https://doi.org/10.1002/ADFM.201809206.
[21] N. Reta, A. Michelmore, C. Saint, B. Prieto-Simón, N.H. Voelcker, Porous silicon membrane-modified electrodes for label-free voltammetric detection of MS2 bacteriophage, Biosens. Bioelectron. 80 (2016) 47–53, https://doi.org/10.1016/J.BIOS.2016.01.038.
[22] M.J. Sailor, Porous Silicon in Practice: Preparation, Characterization and Applications,, 2012, https://doi.org/10.1002/9783527641901.
[23] W. Li, Z. Liu, F. Fontana, Y. Ding, D. Liu, J.T. Hirvonen, H.A. Santos, Tailoring porous silicon for biomedical applications: from drug delivery to cancer immunotherapy, Adv. Mater. 30 (2018) 1703740, https://doi.org/10.1002/ADMA.201703740.
[24] J. Escorihuela, H. Zuilhof, Rapid surface functionalization of hydrogen-terminated silicon by alkyl silanols, J. Am. Chem. Soc. 139 (2017) 5870–5876, https://doi.org/10.1021/JACS.7B01106.
[25] D. Kim, J.M. Zuidema, J. Kang, Y. Pan, L. Wu, D. Warther, B. Arkles, M.J. Sailor, Facile surface modification of hydroxylated silicon nanostructures using heterocyclic silanes, J. Am. Chem. Soc. 138 (2016) 15106–15109, https://doi.org/10.1021/JACS.6B08614.
[26] A.v. Zhukhovitskiy, M.G. Mavros, K.T. Queeney, T. Wu, T. van Voorhis, J. A. Johnson, Reactions of persistent carbenes with hydrogen-terminated silicon surfaces, J. Am. Chem. Soc. 138 (2016) 8639–8652, https://doi.org/10.1021/JACS.6B04962.
[27] C. Pérez-Ràfols, K. Guo, M. Alba, R.J. Toh, N. Serrano, N.H. Voelcker, B. Prieto-Simón, Carbon-stabilized porous silicon as novel voltammetric sensor platforms, Electrochim. Acta 377 (2021) 138077, https://doi.org/10.1016/J.ELECTACTA.2021.138077.
[28] H. Kim, N. Cho, Morphological and nanostructural features of porous silicon prepared by electrochemical etching, Nanoscale Res. Lett. 7 (2012) 408, https://doi.org/10.1186/1556-276X-7-408.
[29] T. Unagami, Oxidation of porous silicon and properties of its oxide film, Jpn. J. Appl. Phys. 19 (1980) 231–241, https://doi.org/10.1143/JJAP.19.231.
[30] L.J. Webb, N.S. Lewis, Comparison of the electrical properties and chemical stability of crystalline silicon(111) surfaces alkylated using grignard reagents or olefins with lewis acid catalysts, J. Phys. Chem. B 107 (2003) 5404–5412, https://doi.org/10.1021/JP0222752.
[31] I.N. Lees, H. Lin, C.A. Canaria, C. Gurtner, M.J. Sailor, G.M. Miskelly, Chemical stability of porous silicon surfaces electrochemically modified with functional alkyl species, Langmuir 19 (2003) 9812–9817, https://doi.org/10.1021/LA035197Y.
[32] E. Mäkilä, L.M. Bimbo, M. Kaasalainen, B. Herranz, A.J. Airaksinen, M. Heinonen, E. Kukk, J. Hirvonen, H.A. Santos, J. Salonen, Amine modification of thermally carbonized porous silicon with silane coupling chemistry, Langmuir 28 (2012) 14045–14054, https://doi.org/10.1021/LA303091K.
[33] T.L. Kelly, T. Gao, M.J. Sailor, Carbon and carbon/silicon composites templated in rugate filters for the adsorption and detection of organic vapors, Adv. Mater. 23 (2011) 1776–1781, https://doi.org/10.1002/ADMA.201004142.
[34] Y. Hishiyama, M. Inagaki, S. Kimura, s. Yamada, Graphitization of carbon fibre/glassy carbon composites, Carbon 12 (1974) 249–258, https://doi.org/10.1016/0008-6223(74)90067-0.
[35] B. Yi, R. Rajagopalan, H.C. Foley, U.J. Kim, X. Liu, P.C. Eklund, Catalytic polymerization and facile grafting of poly(furfuryl alcohol) to single-wall carbon nanotube: preparation of nanocomposite carbon, J. Am. Chem. Soc. 128 (2006) 11307–11313, https://doi.org/10.1021/JA063518X.
[36] M.B. Shiflett, H.C. Foley, Ultrasonic deposition of high-selectivity nanoporous carbon membranes, Science 285 (1999) 1902–1905, https://doi.org/10.1126/SCIENCE.285.5435.1902.
[37] M. Acharya, B.A. Raich, H.C. Foley, M.P. Harold, J.J. Lerou, Metal-supported carbogenic molecular sieve membranes: synthesis and applications, Ind. Eng. Chem. Res. 36 (1997) 2924–2930, https://doi.org/10.1021/IE960769D.
[38] Z. Wang, Z. Lu, Y. Huang, R. Xue, X. Huang, L. Chen, Characterizations of crystalline structure and electrical properties of pyrolyzed polyfurfuryl alcohol, J. Appl. Phys. 82 (1998) 5705, https://doi.org/10.1063/1.366434.
[39] H.A. Katzman, P.M. Adams, T.D. Le, C.S. Hemminger, Characterization of low thermal conductivity pan-based carbon fibers, Carbon 32 (1994) 379–391, https://doi.org/10.1016/0008-6223(94)90158-9.
[40] S. Mrozowski, Proceedings of the Fifth Conference on Carbon, Vol. 2.
[41] a B. Prieto-Simón, C. Saint, N.H. Voelcker, Electrochemical biosensors featuring oriented antibody immobilization via electrografted and self-assembled hydrazide chemistry, Anal. Chem. 86 (2014) 1422–1429, https://doi.org/10.1021/ac401747j;
b D.Y. Chan, A.G. Sega, J.Y. Lee, T. Gao, F. Cunin, F. di Renzo, M.J. Sailor, Optical detection of C2 hydrocarbons ethane, ethylene, and acetylene with a photonic crystal made from carbonized porous silicon, Inorg. Chim. Acta. 422 (2014) 21–29, https://doi.org/10.1016/J.ICA.2014.07.069.
[42] D.Y. Chan, A.G. Sega, J.Y. Lee, T. Gao, F. Cunin, F. di Renzo, M.J. Sailor, Optical detection of C2 hydrocarbons ethane, ethylene, and acetylene with a photonic crystal made from carbonized porous silicon, Inorg. Chim. Acta. 422 (2014) 21–29, https://doi.org/10.1016/J.ICA.2014.07.069.
[43] R.K. Mariwala, H.C. Foley, Evolution of ultramicroporous adsorptive structure in poly(furfuryl alcohol)-derived carbogenic molecular sieves, Ind. Eng. Chem. Res. 33 (2002) 607–615, https://doi.org/10.1021/IE00027A018.
[44] C.J. Anderson, S.J. Pas, G. Arora, S.E. Kentish, A.J. Hill, S.I. Sandler, G.W. Stevens, Effect of pyrolysis temperature and operating temperature on the performance of nanoporous carbon membranes, J. Membr. Sci. 322 (2008) 19–27, https://doi.org/10.1016/J.MEMSCI.2008.04.064.
[45] M.A.T. Jaya, W.M.H.F.W. Harun, M.A. Ahmad, Influence of pyrolysis temperature and heating rate in the fabrication of carbon membrane: a review, J. Appl. Sci. 14 (2014) 1359–1364, https://doi.org/10.3923/JAS.2014.1359.1364.
[46] C.K. Tsang, T.L. Kelly, M.J. Sailor, Y.Y. Li, Highly stable porous silicon-carbon composites as label-free optical biosensors, ACS Nano 6 (2012) 10546–10554, https://doi.org/10.1021/NN304131D.
[47] A. Alvarez-Fernandez, B. Reid, M.J. Fornerod, A. Taylor, G. Divitini, S. Guldin, Structural characterization of mesoporous thin film architectures: a tutorial overview, ACS Appl. Mater. Interfaces 12 (2020) 5195–5208, https://doi.org/10.1021/ACSAMI.9B17899.
[48] T.F. Paes, A.F. Beloto, E.C.D.S. Galvão, L.A. Berni, Simple method for measuring the porosity, thickness and refractive index of porous silicon, based on the Fabry-Pérot interference spectrum, Rev. Brasil. Aplicações Vácuo 35 (2017) 117, https://doi.org/10.17563/rbav.v35i3.1044.
[49] C. Pacholski, M. Sartor, M.J. Sailor, F. Cunin, G.M. Miskelly, Biosensing using porous silicon double-layer interferometers: reflective interferometric fourier transform spectroscopy, J. Am. Chem. Soc. 127 (2005) 11636–11645, https://doi.org/10.1021/ja0511671.
[50] C.K. Tsang, T.L. Kelly, M.J. Sailor, Y.Y. Li, Highly stable porous silicon-carbon composites as label-free optical biosensors, ACS Nano 6 (2012) 10546–10554, https://doi.org/10.1021/NN304131D.
[51] G. Cleland, B.R. Horrocks, A. Houlton, Direct functionalization of silicon via the self-assembly of alcohols, J. Chem. Soc., Faraday Trans. 91 (1995) 4001–4003, https://doi.org/10.1039/FT9959104001.
[52] F. D'Amico, M.E. Musso, R.J.F. Berger, N. Cefarin, G. Birarda, G. Tondi, D. Bertoldo Menezes, A. Reyer, L. Scarabattoli, T. Sepperer, T. Schnabel, L. Vaccari, Chemical constitution of polyfurfuryl alcohol investigated by FTIR and Resonant Raman spectroscopy, Spectrochim. Acta Mol. Biomol. Spectrosc. 262 (2021) 120090, https://doi.org/10.1016/J.SAA.2021.120090.
[53] G. Tondi, N. Cefarin, T. Sepperer, F. D'Amico, R.J.F. Berger, M. Musso, G. Birarda, A. Reyer, T. Schnabel, L. Vaccari, Understanding the polymerization of polyfurfuryl alcohol: ring opening and diels-alder reactions, Polymers 11 (2019) 2126, https://doi.org/10.3390/POLYM11122126.

[54] C.L. Burket, R. Rajagopalan, A.P. Marencic, K. Dronvajjala, H.C. Foley, Genesis of porosity in polyfurfuryl alcohol derived nanoporous carbon, Carbon 44 (2006) 2957–2963, https://doi.org/10.1016/J.CARBON.2006.05.029.
[55] T. Kim, J. Jeong, M. Rahman, E. Zhu, D. Mahajan, Characterizations of furfuryl alcohol oligomer/polymerization catalyzed by homogeneous and heterogeneous acid catalysts, Kor. J. Chem. Eng. 31 (2014) 2124–2129, https://doi.org/10.1007/S11814-014-0322-X.
[56] G. Falco, N. Guigo, L. Vincent, N. Sbirrazzuoli, Opening furan for tailoring properties of bio-based poly(furfuryl alcohol) thermoset, ChemSusChem 11 (2018) 1805–1812, https://doi.org/10.1002/CSSC.201800620.
[57] Z. Wang, Z. Lu, X. Huang, R. Xue, L. Chen, Chemical and crystalline structure characterizations of polyfurfuryl alcohol pyrolyzed at 600 °C, Carbon 36 (1998) 51–59, https://doi.org/10.1016/S0008-6223(97)00150-4.
[58] G. Li, Z. Lu, B. Huang, Z. Wang, H. Huang, R. Xue, L. Chen, Raman scattering investigation of carbons obtained by heat treatment of a polyfurfuryl alcohol, Solid State Ionics 89 (1996) 327–331, https://doi.org/10.1016/0167-2738(96)00352-9.
[59] Z. Wang, Z. Lu, Y. Huang, R. Xue, X. Huang, L. Chen, Characterizations of crystalline structure and electrical properties of pyrolyzed polyfurfuryl alcohol, J. Appl. Phys. 82 (1998) 5705, https://doi.org/10.1063/1.366434.
[60] Z. Wang, Z. Lu, X. Huang, R. Xue, L. Chen, Chemical and crystalline structure characterizations of polyfurfuryl alcohol pyrolyzed at 600°C, Carbon 36 (1998) 51–59, https://doi.org/10.1016/S0008-6223(97)00150-4.
[61] F.F. Bentley, N.T. McDevitt, W.G. Fateley, Infrared and Raman selection rules for lattice vibrations: the correlation method, Appl. Spectrosc. 25 (1971) 155–173. https://opg.optica.org/abstract.cfm?uri=as-25-2-155.
[62] Y.S. Lim, H.S. Kim, M.S. Kim, N.H. Cho, S. Nahm, Chemical and micro-structural changes in glass-like carbon during high temperature heat treatment, Macromol. Res. 11 (2003) 122–127, https://doi.org/10.1007/BF03218341.
[63] D. Kim, J. Joo, Y. Pan, A. Boarino, Y.W. Jun, K.H. Ahn, B. Arkles, M.J. Sailor, Thermally induced silane dehydrocoupling on silicon nanostructures, Angew Chem. Int. Ed. Engl. 55 (2016) 6423, https://doi.org/10.1002/ANIE.201601010.
[64] L. Tang, Y. Wang, Y. Li, H. Feng, J. Lu, J. Li, Preparation, structure, and electrochemical properties of reduced graphene sheet films, Adv. Funct. Mater. 19 (2009) 2782–2789, https://doi.org/10.1002/ADFM.200900377.
[65] R.L. McCreery, Advanced carbon electrode materials for molecular electrochemistry, Chem. Rev. 108 (2008) 2646–2687, https://doi.org/10.1021/CR068076M.
[66] A. Casanova, J. Iniesta, A. Gomis-Berenguer, Recent progress in the development of porous carbon-based electrodes for sensing applications, Analyst 147 (2022) 767–783, https://doi.org/10.1039/D1AN01978C.
[67] C. Punckt, M.A. Pope, I.A. Aksay, On the electrochemical response of porous functionalized graphene electrodes, J. Phys. Chem. C 117 (2013) 16076–16086, https://doi.org/10.1021/JP405142K.
[68] V. Fragkou, Y. Ge, G. Steiner, D. Freeman, N. Bartetzko, A.P.F. Turner, C. Health, V. Building, Determination of the real surface area of a screen-printed electrode by chronocoulometry, Int. J. Electrochem. Sci. 7 (2012) 6214–6220. https://doi.org/10.1016/S1452-3981(23)19475-2.
[69] N. Elgrishi, K.J. Rountree, B.D. McCarthy, E.S. Rountree, T.T. Eisenhart, J. L. Dempsey, A practical beginner's guide to cyclic voltammetry, J. Chem. Educ. 95 (2018) 197–206, https://doi.org/10.1021/ACS.JCHEMED.7B00361.
[70] E.P. Randviir, A cross examination of electron transfer rate constants for carbon screen-printed electrodes using Electrochemical Impedance Spectroscopy and cyclic voltammetry, Electrochim. Acta 286 (2018) 179–186, https://doi.org/10.1016/J.ELECTACTA.2018.08.021.
[71] R.S. Nicholson, Theory and application of cyclic voltammetry for measurement of electrode reaction kinetics, Anal. Chem. 37 (2002) 1351–1355, https://doi.org/10.1021/AC60230A016.
[72] R.S. Nicholson, I. Shain, Theory of stationary electrode polarography. Single scan and cyclic methods applied to reversible, irreversible, and kinetic systems, Anal. Chem. 36 (2002) 706–723, https://doi.org/10.1021/AC60210A007.
[73] I. Lavagnini, R. Antiochia, F. Magno, An extended method for the practical evaluation of the standard rate constant from cyclic voltammetric data, Electroanalysis 16 (2004) 505–506, https://doi.org/10.1002/ELAN.200302851.
[74] J. Salonen, E. Mäkilä, Thermally carbonized porous silicon and its recent applications, Adv. Mater. 30 (2018) 1703819, https://doi.org/10.1002/ADMA.201703819.
[75] K.K. Cline, M.T. McDermott, R.L. McCreery, Anomalously slow electron transfer at ordered graphite electrodes: influence of electronic factors and reactive sites, J. Phys. Chem. 98 (1994) 5314–5319, https://doi.org/10.1021/J100071A023.
[76] K. Guo, M. Alba, G.P. Chin, Z. Tong, B. Guan, M.J. Sailor, N.H. Voelcker, B. Prieto-Simón, Designing electrochemical biosensing platforms using layered carbon-stabilized porous silicon nanostructures, ACS Appl. Mater. Interfaces 14 (2022) 15565–15575, https://doi.org/10.1021/ACSAMI.2C02113.
[77] T. Palaniselvam, H.B. Aiyappa, S. Kurungot, An efficient oxygen reduction electrocatalyst from graphene by simultaneously generating pores and nitrogen doped active sites, J. Mater. Chem. 22 (2012) 23799–23805, https://doi.org/10.1039/C2JM35128E.
[78] J. Wu, Understanding the electric double-layer structure, capacitance, and charging dynamics, Chem. Rev. 122 (2022) 10821–10859, https://doi.org/10.1021/ACS.CHEMREV.2C00097.
[79] D. Qu, Fundamental principals of battery design: porous electrodes, AIP, Conf. 1597 (2014) 14–25, https://doi.org/10.1063/1.4878477.
[80] A. Walcarius, Mesoporous materials-based electrochemical sensors, Electroanalysis 27 (2015) 1303–1340, https://doi.org/10.1002/ELAN.201400628.
[81] P. Chen, R.L. McCreery, Control of electron transfer kinetics at glassy carbon electrodes by specific surface modification, Anal. Chem. 68 (1996) 3958–3965, https://doi.org/10.1021/AC960492R.
[82] P.S. Guin, S. Das, P.C. Mandal, Electrochemical reduction of quinones in different media: a review, Int. J. Electrochem. 2011 (2011) 816202, https://doi.org/10.4061/2011/816202.
[83] B. Brunetti, E. de Giglio, D. Cafagna, E. Desimoni, XPS analysis of glassy carbon electrodes chemically modified with 8-hydroxyquinoline-5-sulphonic acid, Surf. Interface Anal. 44 (2012) 491–496, https://doi.org/10.1002/SIA.3880.
[84] A. Dekanski, J. Stevanović, R. Stevanović, B.Ž. Nikolić, V.M. Jovanović, Glassy carbon electrodes: I. Characterization and electrochemical activation, Carbon 39 (2001) 1195–1205, https://doi.org/10.1016/S0008-6223(00)00228-1.
[85] G.T. Hermanson, Bioconjugate techniques: third ed., Academic Press, Amsterdam, 2013, https://doi.org/10.1016/C2009-0-64240-9.
[86] E. Mäkilä, L.M. Bimbo, M. Kaasalainen, B. Herranz, A.J. Airaksinen, M. Heinonen, E. Kukk, J. Hirvonen, H.A. Santos, J. Salonen, Amine modification of thermally carbonized porous silicon with silane coupling chemistry, Langmuir 28 (2012) 14045–14054, https://doi.org/10.1021/LA303091K.
[87] N. Reta, C.P. Saint, A. Michelmore, B. Prieto-Simon, N.H. Voelcker, Nanostructured electrochemical biosensors for label-free detection of water- and food-borne pathogens, ACS Appl. Mater. Interfaces 10 (2018) 6055–6072, https://doi.org/10.1021/ACSAMI.7B13943.
[88] K.S. Tücking, R.B. Vasani, A.A. Cavallaro, N.H. Voelcker, H. Schönherr, B. Prieto-Simon, Hyaluronic acid–modified porous silicon films for the electrochemical sensing of bacterial hyaluronidase, Macromol. Rapid Commun. 39 (2018) 1800178, https://doi.org/10.1002/MARC.201800178.
[89] Q. Wang, Y. Wen, Y. Li, W. Liang, W. Li, Y. Li, J. Wu, H. Zhu, K. Zhao, J. Zhang, N. Jia, W. Deng, G. Liu, Ultrasensitive electrochemical biosensor of bacterial 16S rRNA gene based on polyA DNA probes, Anal. Chem. 91 (2019) 9277–9283, https://doi.org/10.1021/ACS.ANALCHEM.9B02175.
[90] I. Vlassiouk, P. Takmakov, S. Smirnov, Sensing DNA hybridization via ionic conductance through a nanoporous electrode, Langmuir 21 (2005) 4776–4778, https://doi.org/10.1021/LA0471644.
[91] L. Wang, Q. Liu, Z. Hu, Y. Zhang, C. Wu, M. Yang, P. Wang, A novel electrochemical biosensor based on dynamic polymerase-extending hybridization for E. coli O157:H7 DNA detection, Talanta 78 (2009) 647–652, https://doi.org/10.1016/J.TALANTA.2008.12.001.
[92] J. Deng, C.S. Toh, Impedimetric DNA biosensor based on a nanoporous alumina membrane for the detection of the specific oligonucleotide sequence of dengue virus, Sensors 13 (2013) 7774–7785, https://doi.org/10.3390/S130607774.
[93] A. de La Escosura-Muñiz, A. Mekoçi, Nanoparticle based enhancement of electrochemical DNA hybridization signal using nanoporous electrodes, Chem. Commun. 46 (2010) 9007–9009, https://doi.org/10.1039/C0CC02683B.